ENHANCED LUMINESCENCE PROPERTIES OF PULSED LASER DEPOSITED EUROPIUM ACTIVATED YTTRIUM OXIDE THIN FILMS

By

JAEYOUNG CHOI

A DISSERTATION PRESENTED TO THE GRADUATE SCHOOL
OF THE UNIVERSITY OF FLORIDA IN PARTIAL FULFILLMENT
OF THE REQUIREMENTS FOR THE DEGREE OF
DOCTOR OF PHILOSOPHY

UNIVERSITY OF FLORIDA

2003

To my friends in Gainesville

ACKNOWLEDGMENTS

First, I would like to express my grateful thanks to my advisor and mentor, Dr. Singh for his advice, support, and the freedom to pursue my own research during my years at the University of Florida. Without his drive, I may have never graduated. And I also would like to thank Dr. Pearton, Dr. Abernathy, Dr. Hebard, and Dr. Norton for serving as the members of my supervisory committee as well as for their warm guidance and interest.

I especially would like to thank Han Ho and Joodong for their help with the modeling work and discussions on my results. This dissertation may not have been completed without their assistance. I was very fortunate to have been in the same group. I also thank my fellow group members, past and present, Dr. Kyu-Gong Cho, Dr. Zhan Chen, Dr. Seung-Mahn Lee, Wonseop, Joodong, Hyuksoo, Wonseok, Sanghyun and Suho. They were always willing to lend a hand when I needed it. They also made my stay here in Gainesville very enjoyable. Special thanks are also due to Jung-Sik, Heesun and Kwang-Hoon for their help with luminescence measurements. Finally, I would like to thank all of my friends and family, JongKyung and Wookyuk, as they were very patient and supportive during my stay at UF.

TABLE OF CONTENTS

Page

ACKNOWLEDGMENTS iii

ABSTRACT vi

CHAPTERS

1. INTRODUCTION 1

2. LITERATURE REVIEW 4

   Field Emission Display 4
   Europium – activated Yttrium Oxide (Y_2O_3:Eu) 7
   Cathodoluminescence (CL) 9
   Photoluminescence (PL) 13

3. EXPERIMENTAL PROCEDURE 23

   Target Preparation 23
   Substrate Preparation 23
   Thin Film Phosphor Fabrication by Pulsed Laser Deposition (PLD) 23
   Characterization 24
      X-Ray Diffraction (XRD) 24
      Scanning Electron Microscopy 25
      Optical Profilometry 26
      Photoluminescence (PL) 28
      Cathodoluminescence (CL) 29

4. RESULTS AND DISCUSSION 35

   Anodized Silicon Surface Formation 35
   Y_2O_3:Eu Thin Film Phosphors on Anodized Silicon Surface 38
   Luminescent Properties of Y_2O_3:Eu Thin Film Phosphors 41
      Photoluminescence 41
      Cathodoluminescence 43
   Summary 45

5. MODELING 63

   Assumptions for modeling 64

Surface Roughness of Film 66
Intensity Change by an Angle Change 66
Scattering of Light at Interface 67
Charge Carrier Diffusion and Concentration 69
Modeling of Specular Component of Light 72
Light Propagating in Upward Direction 73
Light Propagating in Downward Direction 73
Light (I_1) Transmitted from Film into Buffer layer 74
Light (I_2) Transmitted Back from Buffer layer into Film 74
Light (I_3) Transmitted from Buffer layer into Substrate 75
Light (I_4) Transmitted Back from Substrate into Buffer layer 76
Summation of Intensities 76
Integration of Specular Component 82
Modeling of Diffuse Component of Light 82
Light Propagating in Upward Direction (Diffuse) 82
Light Propagating in Downward Direction (Diffuse) 83
Summation of Intensities (Diffuse) 84
Integration of Diffuse Component 86
Summation of Specular and Diffuse 86
Predicted and Experimental Results 87
Summary 90

6. CONCLUSIONS 105

LIST OF REFERENCES 107

BIOGRAPHICAL SKETCH 112

Abstract of Dissertation Presented to the Graduate School
of the University of Florida in Partial Fulfillment of the
Requirements for the Degree of Doctor of Philosophy

ENHANCED LUMINESCENCE PROPERTIES OF PULSED LASER DEPOSITED EUROPIUM ACTIVATED YTTRIUM OXIDE THIN FILMS

By

Jaeyoung Choi

December 2003

Chair: Rajiv K. Singh
Major Department: Materials Science and Engineering

The surface roughness of thin film phosphors (TFPs) is one of the factors that affect the brightness of cathodoluminescence (CL). Tailoring the surface roughness of TFPs using various methods can enhance the relatively low brightness of the TFPs. One approach to modifying the surface roughness can be the formation of an anodized silicon surface prior to deposition of TFP. The anodized silicon surface is inherently rough, and thus varying the roughness of the surface can suitably control the roughness of the TFP. This approach has several advantages of lower cost, rapidity and simplicity in wet chemical process.

Another approach to improving the luminescent properties of TFPs can be to insert a buffer layer that is optically favorable for the TFPs and the substrates. In this study, a SiO_2 buffer layer has been investigated to enhance the luminescent brightness. Enhanced luminescence properties were observed from Y_2O_3:Eu films on SiO_2 buffer layered silicon substrates. Due to a smaller refractive index and low absorption characteristics of the buffer layer, a larger amount of total internal reflection in the film and low loss of light intensity during the multiple internal reflections was observed. The light trapped inside the film can escape the film more easily due to a rougher film surface.

A numerical model that was developed from a previous one based on the diffraction scattering theory of light, the steady-state diffusion condition of carriers, and the Kanaya-Okayama's electron beam-solid interaction range satisfactorily explains all the experimental results mentioned above. The model also provides a solid understanding of the cathodoluminescence properties of the TFPs with the effects of other single or multiple luminance parameters. The parameters encountered for the model are surface roughness, buffer layer thickness, electron beam-solid interaction, surface recombination rate of carriers, charge carrier diffusion properties, multiple scattering at the interfaces (air-film, film-buffer layer, buffer layer-substrate, and substrate-air), optical properties of the material, film thickness, and substrate type. The model supplies a general solution in both qualitative and quantitative ways to estimate the luminance properties of the TFPs and it can be utilized to optimize the TFP properties for the application of field emission flat panel displays.

CHAPTER 1
INTRODUCTION

Recent efforts have been made to develop various phosphors for field emission displays (FEDs) that are very thin and compact in comparison to conventional cathode ray tubes (CRTs). Their unique dimensions make them the ideal display media for portable electronic devices. FEDs offer advantages in terms of their wide operating temperature range, wide viewing angle, fast response time, low power consumption, high brightness, high durability, low weight, and scalability [Off95, She98, Hol99, Kor99].

However, currently available phosphors do not have high enough cathodoluminescence (CL) efficiencies at low voltages [She98] whereas low-voltage operation is desirable for portable FEDs due to their relatively low power consumption and easy switching method for the anode [Cou96, Kim97, Vec99].

The use of less efficient phosphors at low voltages requires high current operation that increases the phosphor degradation rate [Vec99]. Y_2O_2S:Eu, which is used as the red primary in the CRT, has been known to degrade under electron bombardment with high current densities and to contaminate the cold cathodes, resulting in fatal damage to FED devices. Therefore, the oxide based phosphors are highly attractive in use of the FED devices and have some advantages in terms of less degradation that make them more desirable materials for FED applications [Tro97]. Among the oxide phosphors, Y_2O_3:Eu is currently one of the leading red phosphor materials for FEDs [Jon99].

On the other hand, there have been some major concerns associated with powder phosphors in terms of debonding, outgassing, and carbon contamination because the field emitter tips are very closely faced (0.2 – 2.0 mm) to the phosphor screen in FEDs. Therefore, thin film phosphors (TFPs) are assumed to be the only answer to solve these challenges.

However, the relatively low efficiency and brightness of the TFPs have prevented them from being used in FEDs so far. The relatively low efficiency of the TFPs compared to powder phosphors can be significantly enhanced by tailoring the surface roughness of the TFPs using various methodologies including variation in processing conditions [Jon97a, b, Jon99], modifying the TFP's surface [Sch93, Lee98], and insertion of a buffer layer between TFP and substrate [Cho97, Cho98a]. It has been experimentally shown that light trapping due to internal reflection from a smooth surface is reduced as the surface becomes progressively rougher [Sch93, Lee98, Yos98, Cho99].

Another method of modifying the surface roughness of TFPs can be the formation of an anodized (or porous) silicon layer to be applied to a Si substrate as a template. This method can be much easier and reproducible because there is no need for an additional buffer layer or change in processing conditions. Anodized silicon is formed by the electrochemical anodization of a silicon wafer [Uhl56, Tur58]. Depending on the doping type, doping level, and anodization conditions, the anodized silicon can have a different morphology with the pore size ranging from several nanometers to tens of microns [Sea92a]. Therefore, the formation of an anodized silicon layer on a silicon substrate has several advantages such as low cost, rapidity and simplicity in wet chemical process, and uniformity on large area substrates.

Aside from modifying the roughness of the TFPs, the insertion of an optically favorable buffer layer between the TFP and substrate serves to enhance the luminescent properties of TFPs. This can help to reduce the light trapping and to improve the light emission from TFPs. In order to avoid trial and error through experiments, it is worth trying to set up a numerical model and predict results theoretically. There have been a few simplified models suggested to predict the brightness of the TFPs [Sch93, Lee98, Cho99, Jon99, Cho03]; however, they did not take into account multilayer effects. Therefore, one of the objectives of this study was to understand the effects of the fundamental parameters influencing the luminescent properties of TFPs with a numerical model developed.

In this dissertation, Chapter 2 presents an overview of the literature survey of related subjects to this research. This includes a brief review of FEDs, an understanding of CL, an outline of the Y_2O_3:Eu phosphor, critical issues in TFP technology, and diffraction-based light scattering at rough surfaces. Furthermore, pulsed laser deposition (PLD) is also briefly introduced. Chapter 3 discusses the experimental procedures and characterization techniques that were used for investigating process parameters of Y_2O_3:Eu TFPs in PLD and for understanding the phosphor properties. Chapter 4 presents and discusses the results of the experiments including surface chemistry of targets and films, microstructural, optical properties, photoluminescence (PL), and cathodoluminescence (CL) studies. Chapter 5 explains the modeling procedures of the fundamental parameters controlling the luminance of TFPs followed by comparisons between the experimental results and the theoretical model. Finally, all the conclusions of the review are presented in Chapter 6.

CHAPTER 2
LITERATURE REVIEW

Field Emission Display

FED is one type of the flat panel displays (FPDs) by the tunneling cold electrons that emit from an array of field emission tips in vacuum when an externally strong electric field (> 5 kV/μm) is applied. Since FEDs and the conventional cathode ray tubes (CRTs) that are widely used by desktop computer monitors and televisions operate on similar principles, FEDs exhibit the strong points of the CRTs such as full color and full gray scale, high brightness, fast response time, wide viewing angle, and wide operating temperature and humidity range [Off95, She98, Kor99]. In addition, FEDs also have the advantages of the FPDs (flat panel displays) with the demand for smaller, lighter, more portable, and less power consuming displays without the magnetic and x-ray radiation as a next generation display [Off95, Hol96, She98, Kor99]. The lap-top computer and palm-top computer markets are dominated by the active matrix liquid crystal display (AMLCD) presently while the plasma display panel (PDP) is leading market sales in large viewing area flat panel displays [Reu00] whereas the AMLCD has many limitations in the areas of viewing angle, temperature range, power consumption, smearing of fast moving video images, and cost [Cat95] and the PDPs are trying to reduce their power consumption and cost [Reu00].

When a strong electric field is applied cold electron tunneling occurs in vacuum from metal and the semiconductor surface [Smi98]. Particularly, when the electric field more than 5 kV/μm is applied to the surface, there is a possibility of electrons' tunneling due to the total potential change, as shown in Figure 2-1 [Hud92]. However, if a flat metal surface emitter was applied to the FED, the problem of the vacuum breakdown could occur due to the whisker formation on the surface at the electric field below 5 kV/μm [Bro64]. Therefore, research on the sharp tip emitter geometry on which electric field is concentrated has been investigated intensively. In the emitter of this pattern, the relationship between the electric field and the electric current density due to the emitted electrons is described by the Fowler-Nordheim (FN) equation:

$$J = \left[A \cdot \frac{(\beta \cdot V)^2}{\Phi} \right] \cdot e^{-\left[\frac{B \cdot \Phi^{\frac{3}{2}}}{\beta \cdot V} \right]} \tag{2.1}$$

where J is the current density, V is the applied voltage, Φ is the work function, A is a function of Φ, B is a constant and β is a geometrical factor dependent on the electrode configuration such that $F = \beta V$, where F is the magnitude of the electric field at the emitting surface. The important thing to notice from this equation is that the electron emission current depends exponentially on the electronic state (as modified by adsorbed gas species), the geometry of the emitting surface and the electrodes of the system through Φ and β, respectively [Sch95].

As shown in Figure 2-2, the electron beam is generated at the emitter tips and is directed to the phosphors on the faceplate, which are excited to produce the luminescence that is seen by the viewer. These emitter tips are part of an emitter tip array that contains millions of emitter tips. At each column/row junction, there are as many as 4,500 emitters. Then by applying a small voltage across the row cathode and the column gate, electrons are emitted from these nano-tips.

The electron emitters (~1μm) for the FED are composed of tens of thousands (depends on the resolution) per pixel and should assure the uniform characteristic which plays an excellent role as the electron source. The pivotal points include what kind of material can be used in fabricating the emitters and how they can be made in order for the electrons to tunnel in a stable way from low voltage and large area. In order to be applied efficiently to the vacuum micro electronics including the FEDs, the essential factors of the field emission devices are the following.

- Uniformity and stability of emission region: The emission region should be defined with tolerance below the sub-micron and should not be deformed while operating.
- Mechanical, chemical, and thermal durability: The device should endure various factors that are the possibilities of happening from vacuum environment, namely ion bombardment, reaction with residual gases, temperature rise, and discharge.
- Low operating voltage: The voltage controlling the emission current should be as low as possible. The material which has low work function could be employed or a method which reduces the distance between gate electrode and tip from the scope where the process is permitted should be considered.
- High emission current value: The induced current value should be as high as possible. At least, the current value (~10 A/cm^2) should be induced to be applied to athe vacuum micro-devices besides FEDs.
- Low energy dispersion of the emitted electrons: The energy dispersion degree of the electrons which are emitted should be comparable to the thermal ion cathode, the value below about 0.5 eV is required.
- Low electric current perturbation: The perturbation and noise of the electric current which is emitted should be enough not to damage the performance of the element.
- Reproducibility of emission characteristics: The characteristics of each device should be uniform and stable whithin the required life-time.
- Simplicity of manufacturing process: The process should be simple enough for yield and productivity to reduce the cost.

Europium – activated Yttrium Oxide (Y_2O_3:Eu)

Europium-doped oxysulfide (Y_2O_2S:Eu) that has an efficiency of 13%, while the reported efficiency value for the oxide is 6.5 - 8%, has been utilized as the traditional cathode ray tube (CRT) red phosphor [Kin70]. The sulfides; however, are known to degrade rapidly under the high current densities required for field emission display technology [Ito89, Swa96]. Therefore, rare earth-activated oxide-based phosphors are likely to emerge as the material of choice for the FED because of their excellent light output and color rendering capabilities [Bla94, Duc94]. Y_2O_3:Eu is currently one of the most promising oxide-based red phosphor systems. Due to a $^5D_0 - {}^7F_2$ transition within europium, Y_2O_3:Eu shows luminescence properties and emits red light with a 611 nm wavelength [Wic64]. Yttrium oxide films have been grown mainly using electron-beam evaporation [Sha91], radio frequency sputtering [Oni90, Cra93, Jan93], and sol – gel techniques [Rao96].

Y_2O_3 has a theoretical density of 5.033g/cm^3. Its unit cell is composed of 16 molecules of 80 atoms. The cation occupies two different crystallographic sites, S_6 and C_2, as seen in Figure 2-4. There is a full layer of C_2 sites with a layer of alternating S_6 and C_2 sites, resulting in 75% of the yttriums in C_2 symmetry and 25% in S_6 symmetry. In S_6 symmetry, the yttrium is in contact with body diagonal vacancies, but in contact with face diagonal vacancies in C_2 symmetry. In both symmetries, the cation is surrounded by 6 oxygens [Mae92]. These sites are, therefore, chemically equivalent but crystallographically different. S_6 symmetry is also denoted in the literature as C_{3i} symmetry.

Y_2O_3:Eu shows a main emission peak in the visible spectrum at 611 nm (red) under cathodoluminescent excitation. This results from a $^5D_0 - {}^7F_2$ transition of the Eu^{+3} site

[Hun85, Bla94]. Figure 2-4 shows such a transition. Eu is a rare earth ion and is characterized by an incompletely filled 4f shell. The $4f^6$ shell is shielded by the filled $5s^2$ and $5p^6$ shells [Bla94, Cho98a]. This shielding allows the Eu ion to retain its atomic character and have energy levels close to that of a free ion [Bla94, Ron98]. As a result, the emission is very sharp at the transmission wavelength [Ron98]. This is also the reason that Eu is usually able to keep its characteristic luminescence, regardless of the host material. There are two possible crystallographic configurations for the phosphor due to transition in the C_2 sites. Energy absorbed into the C_{3i} sites is effectively transferred into the C_2 site for recombination [Hun85]. In the literature, C_{3i} symmetry is often referred to as S_6 symmetry [Jon97c].

Of importance in the Y_2O_3 host is the charge transfer to the luminescent center. The highest occupied levels of the ground state in the host lattice are the 2p orbitals of oxygen, while the lowest unoccupied levels are a mixture of the 3s orbitals of oxygen and the 4d orbitals of yttrium. When electrons are promoted to an excited state under electron bombardment, they can be transferred into the D_5 levels of Eu [Bla94]. The configurational coordinate diagram can be used to represent such a transition. For a fixed central atom, the diagram represents the potential energy (E) curves of the atom as a function of the distance between it and its neighbors (R). Figure 2-5 shows such a diagram. The solid lines in the figure represent the ground states and excited states of the activator, while the dashed line represents another excited state of the activator known as the charge-transfer state. The parabolic shape results from the assumption that the restoring force on the neighboring atoms is proportional to their displacement from equilibrium. The charge - transfer state is one which excited electrons can easily be fed into because of allowed transitions from the ground state of the activator or from the host lattice. The luminescent state is not directly accessible because the transitions are forbidden. In Figure 2-5, the minimum in the charge-transfer band causes excited electrons to be effectively transferred into the luminescent states; that is the case for Y_2O_3:Eu. Due to the location of the charge-transfer band in Y_2O_3:Eu, excited electrons populate the luminescent states, giving this phosphor its high quantum efficiency [Zac97].

Cathodoluminescence (CL)

Luminescence is the emission of light from a solid that is “excited” by some form of energy. The term broadly includes the commonly used categories of fluorescence and phosphorescence. Fluorescence is said to occur where emission ceased almost immediately after withdrawal of the exciting source and where there is no thermal cause, whereas in phosphorescence the emission decays for some time after removal of excitation. The distinction between these so-called types of luminescence is somewhat arbitrary and confusing; for example, many minerals have very long post-excitation decay times. Using the term luminescence and specifying the activating energy as a descriptive prefix avoid confusion. Thus radioluminescence is produced by X-rays, photoluminescence (PL) by light (e.g., ultra-violet), cathodoluminescence (CL) results from excitation by electrons, and thermoluminescence results from heating [Yac90, Bla94].

When energetic electrons bombard certain materials, such as insulators and semiconductors, long-wavelength photons are emitted in the ultraviolet, visible, and infrared regions of the electromagnetic spectrum. This phenomenon, known as cathodoluminescence (CL), is strong enough in certain materials, such as europium doped yttrium oxide (Y_2O_3:Eu), which is known as a red phosphor, to be directly observed by the human eye in an electron-beam instrument equipped with an optical microscope.

When electrons enter a solid (1) the host charge can redistribute to oppose the sudden change in electric field; (2) interactions with the crystal lattice can result in scattering (deviations from the original path); (3) inelastic scattering can result in well-defined energy losses of the incident electron; and (4) such characteristic energy losses can involve single-particle and collective (plasmons) excitations of the host electrons [Pin64]. It is the subsequent relaxation to the ground state between characteristic energy levels of the solid, which produces the photons that are detected as CL.

When an energetic electron beam impinges on a solid surface, a number of physical processes take place. A qualitative picture of the interaction of an electron beam with a solid is shown in Figure 2-6 [Mar88]. The beam is focused to a diameter, d, at the surface. Elastic and inelastic interactions take place within the solid and include such processes as excitation, scattering, absorption, and diffusion. These lead to a steady reduction in the energy of the electrons with depth and an enlargement of the beam. Various secondary emissions are induced throughout the enlarged volume provided the electron energy remains high enough. The various radiations are emitted over a 4π solid angle but only those exiting from one of the sample surfaces are normally observed. The intensity of the emission observed from the surface depends not only on the volume over which it is formed but also on the subsequent interactions within the material. For charged particles the interactions are strong and only those produced very near the surface are emitted. Thus secondary electrons are produced throughout the volume, but only those formed very near the surface point of incidence will be able to escape from the solid. The diameter over which they are produced is only slightly larger than the beam diameter itself. Primary X-rays are produced over the entire region where the electron beam energies remain above the appropriate level, and some of these X-rays will exit, even from their deepest limit of formation. This enlarged diameter, D_1, over which secondary X-rays are observed, is one of the limits to resolution in analyzers that make use of them. Cathodoluminescence is similarly generated over the entire region where the electrons retain greater than a few eV energy, and this region, of diameter D_2, is larger than that over which characteristic X-rays are generated and observed. CL emission is not completely absorbed within the solid and some of that generated even at the greatest depths will be emitted from the surface [Bea72].

The incremental energy lost (dE) over a distance of travel (ds) due to an inelastic collision can be found from the Bethe equation [Eve71, Rao74, Joy89, Yac90, Gue96, Tro97]:

$$\frac{dE}{ds} = \frac{-785\rho Z}{AE} \ln\left(\frac{1.166E}{J}\right) \tag{2.2}$$

where A is the atomic weight in g/mol, Z is the atomic number, E is the electron energy, ρ is the density in g/cm^3, J is the mean ionization potential in eV. The latter is the average energy loss per interaction (for all possible energy loss processes), and for Z>13 it can be expressed as

$$J = 9.76Z + \frac{58.5}{Z^{0.19}} \tag{2.3}$$

These equations have been shown to be accurate for E>6.34 multiplied by the mean ionization potential [Eve71, Rao74, Joy89, Yac90, Tro97,]. Below this energy, the modification by Rao-Sahib and Wittry needs to be considered [Rao74]:

$$\frac{dE}{ds} = \frac{-785\rho Z}{1.2588A\sqrt{EJ}} \tag{2.4}$$

This equation corrects for the low energy region while mimicking the behavior of the original Bethe equation at high energy. This new equation can be used for energies as low as approximately 500 V. Attempting to reduce this limit even further, Joy and Luo suggested a new expression for the mean ionization potential using an energy dependent term [Joy89, Czy90, Tro97]:

$$J' = \frac{J}{1 + k\left(\frac{J}{E}\right)} \tag{2.5}$$

where J' is the new mean ionization potential, J is still the average energy loss per interaction, and k is a fitting parameter. The constant k varies from 0.7 to 0.9, but it is usually around 0.85.

The stopping power equations cited above provide a measure of how the electrons lose energy in the solid, but they do not give an accurate indication of the interaction volume. During the electron's trip through the lattice, it will also undergo elastic collisions. These will not result in an energy loss, but rather will lead to a change in the direction of the electron's travel. Equation 2.1 can be integrated to find the length of an individual electron "random walk" trajectory. This is known as the Bethe range.

However, the interaction volume will be much smaller due to scattering. Typically, the interaction volume is known as the Gruen, electron beam, or penetration range. It can be expressed as

$$R_e = \left(\frac{k'}{\rho}\right) E_0^{\alpha} \tag{2.6}$$

where ρ is the density, E_0 is the electron beam energy, k' depends on the atomic number and is a function of energy, and α depends on the atomic number and E. Various equations have been given for the solution to this equation, but Kanaya and Okayama proposed the one most widely accepted

$$R_e = \left(\frac{0.0276A}{\rho Z^{0.889}}\right) E_0^{1.67} \tag{2.7}$$

measured in µm, where E_0 is in keV, A is in g/mol, ρ is in g/cm^3, and Z is the atomic number [Yac90]. Figure 2-7 demonstrates how this interaction volume moves deeper into the material as the beam energy is increased. As shown in this figure, d represents the incident beam diameter, L is the depth of CL generation volume, D_1 is the diameter of where secondary X-rays are generated, and D_2 represents the full diameter to which CL is generated [Mar88]. Incident beam energy is increasing from A to B to C. This also demonstrates how the interaction volume moves closer to the surface as the beam energy is decreased. When surface recombination is considered, the interaction volume in A will clearly have a stronger influence from the surface than that in C. As a result, surface effects become more pronounced at lower beam voltages.

Photoluminescence (PL)

PL refers to the emission resulting from an optically stimulated material. Examples of PL in real life include the brightness of white paper or shirts or in the light from the coating on a fluorescent lamp. The detection and analysis of this emission are widely employed as an analytical tool due to its sensitivity, simplicity, and low cost. Sensitivity is one of the advantages of the PL technique, allowing very small quantities (nanograms) or low concentrations (parts-per-trillion) of material to be analyzed.

Photoluminescence is a technique that allows for a mainly qualitative understanding of a material; however in cases where conditions are precisely controlled, some quantitative measurements are possible, for example particularly for organic materials, wherein the compound of interest can be dissolved in an appropriate solvent and examined either as a liquid in a cuvette or deposited onto a solid surface like silica gel, alumina, or filter paper.

The PL can be classified into two kinds of major types, namely intrinsic and extrinsic luminescence. There are three kinds in the intrinsic such as band-to-band luminescence, exciton luminescence, and cross-luminescence. The latter is divided into unlocalized and localized types, depending on whether excited electrons and holes of the host lattice participate in luminescence processes or whether the luminescence excitation and emission processes are confined to localized centers. Some of the information that can be gleaned from PL measurements includes compound identification, band gap, impurity binding energy, quantum well width, impurity species, Fermi energy, and carrier/doping density [Bru92].

The following equipments are needed for the PL system: 1) A light source, usually a tunable dye laser, 2) a sample holder, which includes a cryostat and optics to focus the light onto the sample, 3) collection optics and a scanning monochromator, and 4) an optical detector. During a PL measurement a fixed wavelength light source is focused on a sample. The interaction of the laser with the semiconductor crystal causes electrons to be excited to higher energy levels. Depending on how the electron relaxes back to a lower energy state, light can be emitted from the sample. The light is collected and passed through the scanning monochromator and the wavelengths of the luminescence are examined [Bru92].

There are a number of PL applications including compositional analysis, trace impurity detection, spatial mapping, structural determination (crystallinity, bonding, layering), and the study of energy-transfer mechanisms. In particular, semiconductor and insulator applications can be emphasized because these areas have received the most attention with respect to surface-related properties (i.e., thin films, roughness, surface treatment, interfaces), as opposed to primarily bulk properties. The common modes of the analysis are spectral emission analysis, excitation spectroscopy, time-resolved analysis, and spatial mapping.

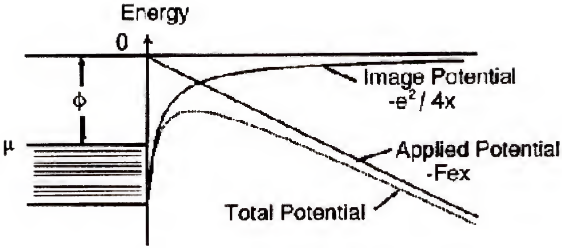

Figure 2-1. Potential energy curves for an electron near a metal surface [Hud92].

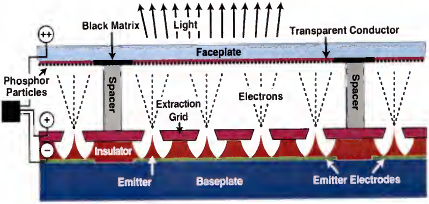

Figure 2-2. Cross section schematic of a typical field emission display of FED.

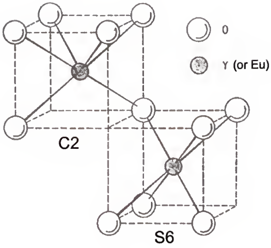

Figure 2-3. Two different octahedral sites, C_2 and S_6, which can be occupied by yttrium or europium ion in the Y_2O_3:Eu crystal structure [And70].

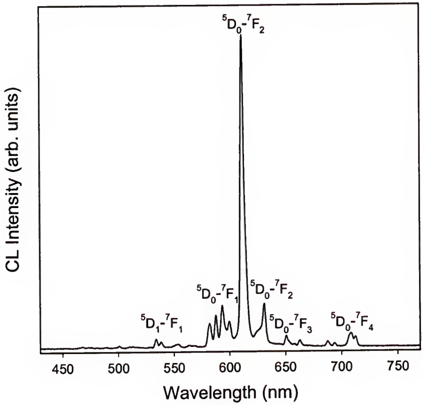

Figure 2-4. CL spectrum of Y_2O_3:Eu phosphor showing different peaks and intensities induced by either magnetic ($^5D_1$-$^7F_1$, $^5D_0$-$^7F_1$) or electric (^5D_o-$^7F_{2\text{-}4}$) dipole transition [Cho98a].

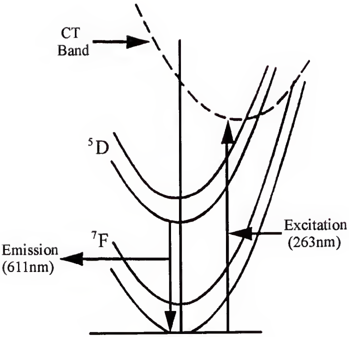

Figure 2-5. The dashed curves represent the charge – transfer (CT) state. The CT state helps feed the emissive ^{5}D levels because of its position relative to the ^{7}F ground state found in Y_2O_3:Eu.

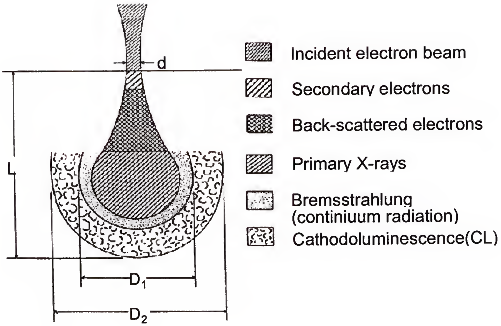

Figure 2-6. Qualitative representation of an electron beam interaction with a solid. Shown are d which represents the incident beam diameter, L is the depth of CL generation volume, D_1 is the diameter of where secondary X-rays are generated, and D_2 represents the full diameter to which CL is generated [Mar88].

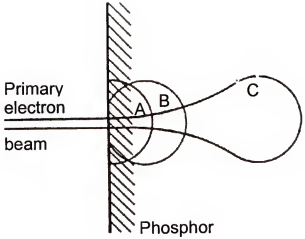

Figure 2-7 Electron penetration in a phosphor at various beam energies. Incident beam energy is increasing from A to B to C. This also demonstrates how the interaction volume moves closer to the surface as the beam energy is decreased. When surface recombination is considered, the interaction volume in A will clearly have a stronger influence from the surface than that in C. As a result, surface effects become more pronounced at lower beam voltages.

CHAPTER 3
EXPERIMENTAL PROCEDURE

Target Preparation

A conventional method of making PLD target was used to prepare a europium-activated yttrium oxide phosphor target. The powder, a chemical formula $(Y_{0.97}Eu_{0.03})_2O_3$, Y_2O_3:Eu, (Osram Sylvania Inc.), was cold pressed into a 1 inch diameter pellet.

The Y_2O_3:Eu pellet was sintered at 1400 °C for 24 hours in air. The chemical composition and homogeneity of the final target was examined by using elemental analysis with an Auger electron spectrometer (AES) and an energy dispersive x-ray spectrometer (EDS)

Substrate Preparation

Y_2O_3:Eu thin films were deposited onto bare and porous silicon substrates by pulsed laser deposition. Also, a thermally grown silicon dioxide layer was formed on both types of substrates before the thin films were deposited. The substrates were ultrasonically degreased in acetone and methanol for 5 minutes each. They were then rinsed in de-ionized (DI) water and blown dry with nitrogen gas. The porous silicon layer was made by electrochemical etching with a dilute HF solution.

Thin Film Phosphor Fabrication by Pulsed Laser Deposition (PLD)

Yttrium oxide doped with europium (Y_2O_3:Eu) thin films were created by PLD in a vacuum chamber where a rotating Y_2O_3:Eu solid target was ablated by incident KrF pulsed excimer laser beam with a wavelength of 248 nm. Pulse frequencies between 1 and 30 Hz were possible, but all films were deposited at 10 Hz. The substrates were mounted on the faceplate of a substrate heater placed parallel to the target surface. A schematic illustration shown in Figure 3-1 represents the PLD system used for fabricating the Y_2O_3:Eu TFPs. By adjusting the lens-to-target distance, laser beam spots with controlled sizes were achieved.

Ultra high purity (5 nines) oxygen from compressed gas cylinders was used to grow films at oxygen environment in the chamber. The gas was introduced into the vacuum system using a needle valve. Throttling the turbo pump, using the gate valve to achieve the desired pressure, regulated the pressure.

The processing conditions to fabricate Y_2O_3:Eu TFPs used were laser energy density of 1.0 (J/cm^2), repetition rate of 10 Hz, oxygen pressure of 50 mTorr, distance from target to substrate of 5 cm, and substrate temperature of 700 °C. The temperatures of the substrates were controlled and monitored using a programmable thermocouple temperature controller and a pyrometer.

Characterization

The films were characterized using a variety of analytical techniques including x-ray diffraction (XRD), scanning electron microscopy (SEM), optical profilometry, photoluminescence (PL), and cathodoluminescence (CL).

X-Ray Diffraction (XRD)

X-ray diffraction was the primary technique used for Y_2O_3:Eu phase and crystallinity identification. A Phillips model APD 3720 x-ray diffractometer was operated at 40 kV and 20 mA to generate Cu Kα radiation of $\lambda = 1.5406$ and 1.5444 Å. A collimated beam of X-rays was incident on a specimen and was diffracted by the crystalline phases in the specimen according to Bragg's law (λ=2d sinθ, where d is the spacing between atomic planes in the crystalline phase). The intensity of the diffracted X-rays was measured as a function of the diffraction angle 2θ and the specimen's orientation.

Scanning Electron Microscopy

The Scanning Electron Microscope (SEM) used in this research was a JEOL JSM-6335f field emission SEM. A field-emission cathode in the electron gun of a scanning electron microscope provides narrower probing beams at low as well as high electron energy, resulting in both improved spatial resolution and minimized sample charging and damage. The SEM uses secondary electrons produced as a result of electron-beam solid interactions to produce a surface topographic and defect image of the sample.

Thermoelectrons are emitted from the surface of metals, oxides, and borides when they are heated to a high temperature. Conventional thermionic electron guns make use of this thermionic emission. On the other hand, a field emission takes place on the surface of a sharp-pointed emitter made of metals, oxides or carbides when a strong electric field is present at the surface. Field emission electron guns make use of this field emission. Many field emission electron guns are now used as electron sources in electron microscopes because of their high brightness.

For a field emission electron gun, a voltage of several thousand volts is applied between the extraction electrode and the cathode, which has a sharp-pointed tungsten metal tip. Since the tip has a curvature radius of about 100nm, a strong electric field of about 10 MV/cm is usually created at the cathode tip and electrons are emitted from the tip by the tunnel effect. The amount of electrons emitted greatly depends on the work function of the cathode surface. When gas molecules are adsorbed on the cathode surface, the amount of electrons emitted changes with the work function.

Once the electron beam strikes the sample, secondary and backscattered electrons are created. These electrons are separated according to their energies. Electrons that are emitted from the sample with energies below 50 eV are the secondary electrons while those with energies above 50 eV are the backscattered electrons. The secondary electrons are used to obtain SEM images. When the electron beam is rastered across the sample, a detector collects the emitted secondary electrons, and the output can be used to modulate the brightness of a cathode ray tube (CRT) whose *x*- and *y*-inputs are driven in synchronism with the x-y voltages rastering the electron beam across the sample. In this way, an image is produced on the CRT; every point that the beam strikes on the sample is mapped directly onto a corresponding point on the screen [Bru92].

Optical Profilometry

Interferometric optical microscopic profilers are often used for the measurement of surface microstructure.

An optical profiler, shown in Figure 3-2, can be thought of as basically a microscope combined with an interferometer. An illumination source, traditionally a tungsten halogen bulb, is coupled to an optical system with a variety of interferometric microscope objectives. The choice of objective depends upon the test surface and the size of the features of interest. The interferometer splits a single source beam of light into two separate beams. One beam is reflected from the object under test and the other beam is reflected from a high-quality reference mirror. The two beams recombine to form a pattern of interference "fringes" (Figure 3-3), the intensity of which is recorded by a CCD camera. The reference surface is translated relative to the test surface such that every point on the surface passes through focus. Throughout the scan, a series of intensity data frames is recorded. Finally, these frames are analyzed using various techniques to determine the height of each point on the surface.

Two techniques have traditionally been used to determine surface heights from the recorded intensity data. Phase Shifting Interferometry (PSI) produces topographic data with extremely low noise and sub-nanometer vertical resolution. PSI is typically used to characterize high-quality surfaces such as optical quality surfaces and coatings, dense wavelength-division-multiplexing filters, wafers, and so on. Short measurement time (less than 0.5 sec.) makes PSI particularly appropriate for high-volume automated quality control. PSI is limited to surfaces with discontinuities typically less than 160nm.

Vertical Scanning Interferometry (VSI), also known as white-light or coherence-sensing interferometry, is based on the detection of the peak contrast of the fringes. VSI is used to characterize surfaces with higher roughness and/or discontinuities, such as steps, cavities, islands, and so on. Heights up to several millimeters can be resolved, though measurement time is longer (several seconds to a minute) due to the added vertical scan length. VSI methods avoid the height and slope limitations of PSI techniques, measuring steps to nearly one centimeter, but they typically sacrifice some accuracy and noise rejection. An optical profiler measures a relatively large surface area (up to approx. 50 mm^2) in a single scan, enabling dramatically faster measurement speed than raster-scanning techniques such as stylus profilometry or confocal microscopy. Stitching algorithms further increase the field of view, allowing multiple measurements to be combined into a single, large dataset. Measurement speed ranges up to 100 microns/second, depending on the desired vertical resolution.

The optical profiler has many advantages over other surface and film testing devices. First, the profiler does not require special sample preparation. It also uses nondestructive techniques, and measurement time is very fast since measurement occurs not point-by-point, but over the whole field of view of the microscope during a single scans. The optical profiler achieves sub-nanometer and nanometer level vertical resolutions while still offering lateral resolution of a few hundred nanometers that is typical for optical microscopes.

Photoluminescence (PL)

Photoluminescence (PL) is the emission of light as a result of optical stimulation. Specifically, one measures the emitted intensity as a function of emission wavelength. The sample being investigated absorbs light from a monochromatic source such as a laser and the absorbed energy results in electron excitation from the ground state into higher energy bands (typically the conduction band), or to quasi bands/defect states in the band gap. Excited electrons may loose a part of their energy by relaxing to the energy minimum of the excited state via non-radiative transitions. After spending a system-dependent time in the excited state, electrons may revert to the ground state by any of the radiative pathways, resulting in photoluminescence. Thus, information pertaining to the band-gap or the position of defect emitting states within the band-gap can be extracted under certain circumstances.

The geometric arrangement for PL measurement used in this study is schematically illustrated in Figure 3-2. Continuous wave excitation was provided by a 325 nm HeCd laser. After passing through a narrow band-pass filter and an iris used to remove the laser sidebands and stray light respectively, the laser beam was focused onto the sample using a quartz lens. Samples were mounted on a XYZ positioner. The light generated by PL was then collected by a lens array as shown in Figure 3-2 and focused onto the entrance slit of an Instruments SA, Inc. HR-320 monochromator. A long-pass filter with a 50% cutoff wavelength at 350 nm was placed at the entrance to the monochromator in order to prevent any scattered laser light from entering. After traversing the monochromator with a grating of appropriate blaze wavelength (660 nm), the light impinged upon a cooled Hamamatsu R943-02 GaAs photomultiplier tube where its intensity was measured.

Cathodoluminescence (CL)

CL was excited by a primary electron beam from a EGPS- 7H Kimball Physik electron gun with energies from 0.5 to 5 keV and currents from 31.4 nA to 314 nA. The spot size was 2 mm in diameter and thus the corresponding current density was in a range of 1 to 10 $\mu A/cm^2$. The sample current was determined by biasing the electrically isolated sample carousel with a 120 volt battery with an ammeter in series to ground. CL properties were measured using an Ocean Optics S2000 fiber optic spectrometer with a charge-coupled device (CCD) detector attached to the personal computer. Figure 3-3 shows a schematic illustration of the CL measurement system. TFPs are excited by e-beams from the electron gun (e-gun), and the emitted light is detected by the two photo-cameras attached to the PC controller to give brightness data.

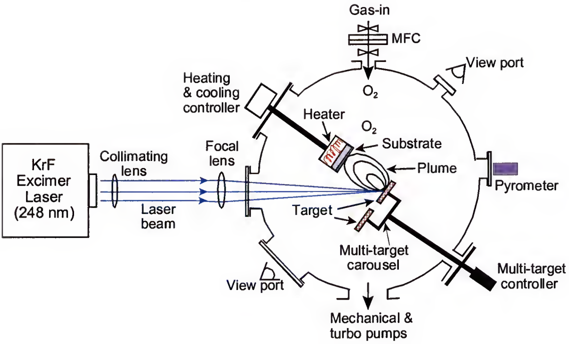

Figure 3-1. Schematic illustration of 248 nm KrF excimer PLD system.

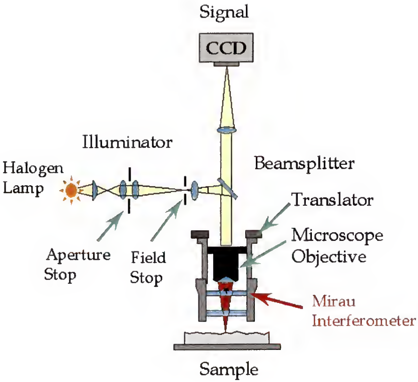

Figure 3-2. Example of a white light optical profiler.

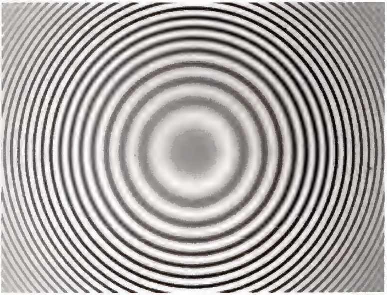

Figure 3-3. Interference fringes on a spherical surface.

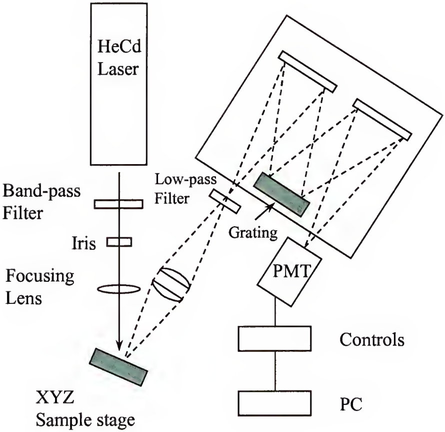

Figure 3-4. Schematic illustration of the PL measurement system.

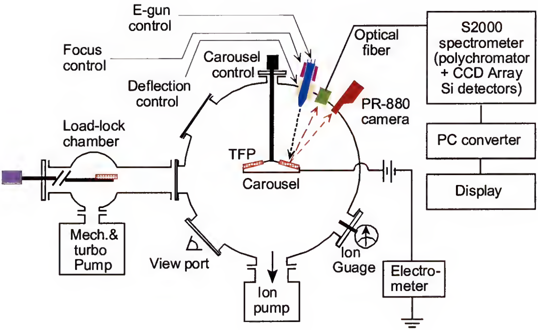

Figure 3-5. Schematic illustration of the CL measurement system.

CHAPTER 4
RESULTS AND DISCUSSION

Microstructure and surface images of anodized silicon substrates and Y_2O_3:Eu films grown by PLD are presented to investigate the effects of the surface roughness on the luminescence properties of thin film phosphors. Anodized silicon substrates that have various surface roughness values were formed electrochemically in aqueous HF solutions with various concentrations. Varying the roughness of the substrate can duly control the roughness of the thin film phosphors on the substrates. It was found that increased surface roughness of the thin film phosphors increased the luminescence intensities. The increase in roughness was accomplished by increasing the roughness of the anodized silicon substrates.

Y_2O_3:Eu films were also deposited on bare silicon surfaces and thermally grown silicon dioxide layers to investigate the effects of other optical parameters affecting the luminescence properties of the thin film phosphor.

Luminescence data from both PL and CL will be related to the thin film phosphor's roughness and the role of thermally grown silicon dioxide buffer layer on silicon substrates.

Anodized Silicon Surface Formation

The goal of changing surface roughness of silicon substrates was accomplished by anodizing a silicon surface in an aqueous HF solution by changing HF concentration and applied potential values.

Anodized (porous) silicon is known to form during electrochemical dissolution of silicon in HF-based solutions. The silicon wafer serves as the anode and the cathode is made of platinum or any HF-resistant and conducting material.

The exact dissolution chemistries of silicon are still unclear and different mechanisms have been proposed. Turner [Tur58], and Memming and Schwandt [Mem66] have proposed the following overall reaction for the dissolution of silicon.

$$Si + 2HF + \lambda h^+ \rightarrow SiF_2 + 2H+ + (2 - \lambda)e^- \qquad (4.1)$$

$$SiF_2 + 2HF \rightarrow SiF_4 + H_2 \qquad (4.2)$$

$$SiF_4 + 2HF \rightarrow H_2SiF_6 \qquad (4.3)$$

where h^+ and e^- are the exchanged hole and electron, respectively, and λ is the number of charges exchanged during the elementary step.

Some parameters, such as the substrate crystallinity and orientation, the shape of the anodic current (pulsed or continuous), external magnetic field, etc., can affect the anodized silicon formation. Also, all the properties of an anodized silicon layer, such as porosity, thickness, pore diameter, microstructure, are strongly dependent on the anodization conditions. These conditions include HF concentration, pH of the solution and its chemical composition, temperature, anodization duration, stirring conditions, and illumination (or not) during anodization. Optimum control of the fabrication and reproducibility are only possible if all the parameters listed above are taken into account. In this study, in order to give roughness variation in anodized silicon surfaces, only HF concentration and applied potential values were considered using n-type silicon wafers for the simplicity of the processing.

Figures 4-1 (a) – (d) show SEM micrographs of anodized n-type silicon surfaces that were electrochemically treated in aqueous HF. The concentrations of electrolyte solutions were 1.0 %, 1.0 %, 5.0 %, and 10.0 % HF, respectively, and the potential values were 1 V in (a) and 5 V in (b) – (d). The current density was around 100 nA. The reaction time was 12 hours. Two-inch diameter n-type silicon wafers with 1 – 10 Ohm·cm resistivity were used. As a whole, the surfaces became roughened with increasing the concentration of the electrolyte solution and the potential applied. No pores were observed, but the surface became roughened on the anodized silicon surface treated in 1.0 % aqueous HF solution at 1 V as shown in Figure 4-1 (a). The formation of small pores was initiated and the surface also became roughened in Figure 4-1 (b), the surface that was treated in 1.0 % HF electrolyte solution at 5 V. The size of the pores was around 100 nm. The neighboring pores were merged and became deeper as the pores propagated laterally and vertically as shown in Figure 4-1 (c) and (d) as the concentration of the electrolyte solution is increased. Generally, the anodization of (100) oriented silicon wafers can generate pores of square shape whilst (111) oriented wafers can exhibit triangular shaped pores [Can87]. However, square shaped pores are not clearly distinguished from these SEM images even though (100) oriented silicon wafers were used in this study. This might be related to the depth of the anodized silicon layer. Most porous silicon layers are a few μm deep [Can87], and in the most general sense a "pore" is an etch pit whose depth, d, exceeds its width, w [Rou94]; however; as will be seen from SEM cross-sectional views the depth of the anodized silicon surfaces used in this study was smaller than 1 μm. Therefore, the anodized silicon surfaces here are rough surfaces of silicon by anodizing in aqueous HF solution rather than porous ones.

Figures 4-2 (a) – (d) show surface images from an optical profilometer. The measured RMS roughness values of the anodized silicon surfaces shown in Figure 4-1 were ~10 nm, ~20 nm, ~30 nm, and ~340 nm, respectively.

Figures 4-3 (a) – (d) show the variations in the RMS roughness of the anodized silicon surfaces with increase in the applied potential and the concentration of aqueous HF solutions. The roughness values of the surfaces were increased with the concentration of the aqueous HF solutions and the potential applied. The roughness on the anodized silicon surface treated in 10 % HF solution at 5 V showed the highest value among the surfaces while the surface treated in 1 % HF solution at 1 V showed the lowest roughness.

For n-type silicon, the applied potential is dropped predominantly across the space-charge region on the silicon side [Gas 89] and the characteristic pore morphology has been explained in terms of a tunneling mechanism involving electron injection at the pore base due to field concentration [Sea92b]. Therefore, it is deduced that the concentration and the applied potential will influence pore morphology on n-type silicon. Generally, an increase in the pore diameters accompanies and increases in the anodization potentials for both n- and p-type silicon although the effect is more pronounced for the larger pore diameters formed in n-type silicon [Smi92].

Y_2O_3:Eu Thin Film Phosphors on Anodized Silicon Surface

Shown in Figure 4-4 (a) and (b) are the XRD patterns of the Y_2O_3:Eu thin film phosphor grown on anodized silicon and the target used in the growth, respectively. This indicates that the target, pressed from europium activated yttrium oxide powder and sintered at 1400 °C for 24 hours, material is preferentially aligned in the [222] direction, and the phosphor film deposited at growth temperature of 700 °C in 50 mTorr also showed the [222] preferred direction. This means the [222] direction of the thin film phosphor remained the preferred orientation as the target was ablated. This is consistent with data reported earlier in which stronger (222) peaks were detected from Y_2O_3:Eu films on glass substrates deposited at 400 °C and 600 °C, along with peaks from higher Miller indices planes and similar results were also obtained from the films grown on (100) silicon and c-axis sapphire [Jon99]. It is noted that for the yttrium oxide/silicon system, the (100) silicon peak was at 69°, which is not plotted on these graphs.

Shown in Figure 4-5 (a) – (d) are SEM micrographs of the Y_2O_3:Eu thin film phosphors with the RMS roughness values of ~60 nm, ~120 nm, ~240 nm, and ~650 nm, respectively, grown on the anodized silicon surfaces. The presence of an anodized silicon layer on the silicon substrate had a strong effect on the film morphology and roughness as illustrated by the SEM micrographs of Y_2O_3:Eu films on the anodized silicon substrates, and the faceted structure on these films seen in these SEM images arose from the crystal structure of Y_2O_3:Eu films. The pyramidal faceted shape of the Y_2O_3:Eu grains is a characteristic of its fluorite body-centered-cubic crystallographic structure in which each cation is surrounded by eight anions located at the corners of a cube [Wil93, Bla94].

The SEM cross-sectional views of the Y_2O_3:Eu films on less (RMS ~60 nm) and more (RMS ~650) roughened anodized silicon substrates are shown in Figure 4-6 (a) and (b), respectively. The cross-sectional images show that the Y_2O_3:Eu thin films have thickness of ~1.0 μm. As shown in Figure 4-6 (b), the interface between the thin film phosphor and the anodized silicon surface looks very irregular and rough; however, the film was deposited conformally along the profile of the rough surface on the anodized silicon.

The roughnesses of these thin films are shown in images from an optical profilometer of the Y_2O_3:Eu thin film phosphor on the anodized silicon surfaces, Figure 4-7. The measured RMS values of the films were ~60 nm, ~120 nm, ~240 nm, and ~650 nm in Figure 4-7 (a) ~ (d), respectively. The higher roughness of the Y_2O_3:Eu thin films grown on the anodized silicon substrates resulted from the presence of the inherently rough surface of the anodized silicon substrates.

Shown in Figure 4-8 (a) ~ (c) and 4-9 (a) ~ (b) are SEM micrographs of plan and cross-sectional views of the Y_2O_3:Eu thin film phosphors grown on anodized silicon surfaces with a SiO_2 buffer layer. The morphologies of Y_2O_3:Eu thin film phosphors on the anodized silicon with a SiO_2 buffer layer were not much different from the films on the anodized silicon without the buffer layer as shown in Figure 4-5. The thickness of the films was also ~1 μm by the cross-sectional images, and ~0.3 μm thickness of the SiO_2 buffer layer underneath the Y_2O_3:Eu film was seen in the figure.

The measured roughness values of these thin films are shown in Figure 4-10 (a) – (c). This figure shows images from an optical profilometer of the Y_2O_3:Eu thin film phosphor on the anodized silicon surfaces. The measured RMS values of the films were ~50 nm, ~210 nm, and ~630 nm in Figure 4-10 (a) to (c), respectively.

The ultimate objective of increasing the roughness of the thin film phosphors by surface modification using the anodized silicon substrates was achieved. Surface modification has previously been accomplished by changing the repetition rate [Cha90], by post deposition laser processing [Fol94], by processing conditions [Jon97a, b, Jon99], by modifying the thin film phosphor's surface [Sch93, Lee98], or by addition of a buffer layer between TFP and substrate [Cho97, Cho98a]. This is; however, the first report of intentionally utilizing the anodized silicon surfaces as a template that has RMS roughness values up to a few hundred nm.

Luminescent Properties of Y_2O_3:Eu Thin Film Phosphors

Photoluminescence

The primary intent of this study was to investigate the effects of changing surface roughness on the PL and CL brightness of Y_2O_3:Eu thin films grown on the anodized silicon surfaces.

The PL spectra recorded from the Y_2O_3:Eu thin film phosphors deposited on anodized silicon surfaces that have different roughness values are shown in Figure 4-11. For comparison, the PL spectrum recorded from Y_2O_3:Eu film grown on bare silicon is also shown in this graph. This figure shows typical photoluminescence spectra of a Y_2O_3:Eu film. The radiation was dominated by the red emission peak at 611 nm which is a $^5D_0 - {}^7F_2$ transition. Some broader peaks from the PL spectra in Figure 4-11 were caused by the lower resolution of the PL spectrometer. All of the Y_2O_3:Eu films were ~1 μm thick in order to exclude any thickness effect on PL intensity. The Y_2O_3:Eu film on the anodized silicon that has RMS roughness value of ~650 nm showed more than 6 times higher PL brightness than the film on bare silicon substrate that has ~20 nm of RMS roughness.

The realization of Y_2O_3:Eu thin film phosphors with higher PL brightness by means of an anodized silicon layer on the substrates is attributed to more outcoupling of light due to reduced internal reflection, increased elastic scattering of the excitation beam, and increased UV – solid interaction volume due to increased effective radiation area

[Jon97a, Cho97, Cho98a]. These effects are caused predominantly by rough anodized silicon surface. As mentioned above, the RMS roughness of the Y_2O_3:Eu films on anodized silicon substrates was ~30 times larger than that on the bare silicon substrate. Therefore, due to higher surface roughness, the process of internal reflection was reduced and the incident beam was scattered more by the lattice, resulting in improved visual brightness from the Y_2O_3:Eu films on anodized silicon substrates [Cho97, Cho98a].

Another approach to improve the luminescent intensity of thin film phosphors on silicon substrates is to insert an optically favorable buffer layer such as silicon dioxide between the phosphor layer and the substrate without any roughness effect. Shown in Figure 4-12 are PL intensities from the Y_2O_3:Eu films with and without a SiO_2 buffer layer between the thin film phosphor and bare silicon substrate demonstrating an increase of PL intensity as the SiO_2 layer is inserted. Thicknesses of the Y_2O_3:Eu thin films on both substrates and the SiO_2 buffer layer are 1.0 and 0.3 μm, respectively. In this figure, the Y_2O_3:Eu thin film on a bare silicon substrate with a SiO_2 buffer showed ~3 times higher PL intensity than that of the film on the bare silicon substrate without the buffer layer even though the RMS roughness of the Y_2O_3:Eu thin films was the same (~20 nm).

The SiO_2 layer has a smaller refractive index ($n = 1.46$) than the refractive index of the Y_2O_3:Eu film ($n = 1.93$) and a lower absorption coefficient ($\alpha = 0.07\ mm^{-1}$) characteristic than that of the film ($\alpha = 5\ mm^{-1}$). The smaller refractive index gives a larger amount of internally reflected light in the film and this internally reflected light can get out of the film more easily as the film is rougher [Sin02]. The low absorption characteristic of visible light decreases absorption during multiple internal reflections and travel through the substrate. These two combined effects may result in better PL properties for the Y_2O_3:Eu thin films on SiO_2 buffer layer.

Cathodoluminescence

In order to investigate the CL properties of the Y_2O_3:Eu thin film phosphors on silicon substrates, the thickness of the films were adjusted to 1 μm to exclude any thickness effect on CL intensity. It was reported that the CL intensity increased very rapidly and then saturated at around 1 μm film thickness indicating that increasing film thickness greater than 1 μm is not very advantageous to get more CL brightness for the Y_2O_3:Eu thin film phosphors, and it was shown that very small differences among the CL intensities before saturation and slightly higher intensities with increase of the diffusivity of an electron (D) value after 1 μm [Cho00]. Since the initial intensities are directly proportional to the number of charge carriers in a thin film phosphor, the charge carrier diffusion is an important part of CL generation process over the electron beam – solid interaction range.

The cathodoluminescence intensities of the Y_2O_3:Eu thin film phosphors deposited on anodized silicon surfaces with various roughness values are shown in Figure 4-13. It can be noted from this figure that as the RMS roughness of Y_2O_3:Eu films on anodized silicon surface is increased, the CL brightness increases at all of the voltages measured. This increased brightness from the films on anodized silicon surfaces is associated with the surface roughness mostly caused by the formation of the anodized silicon surface layer. A similar observation was obtained in the PL brightness and this phenomenon was also discussed above. As can be seen from Figure 4-13, the CL intensity of the film increases with the increase in electron energy applied. The increase in CL brightness with an increase in electron energy is attributed to deeper penetration of electron into the film body. The deeper penetration of electrons into the Y_2O_3:Eu film body results in an increased electron – solid interaction volume in which excitation of Eu^{+3} ions, responsible for light emission, takes place. Therefore, an increase in interaction volume, which effectively determines the generation of light inside the film body, with an increase in electron energy brings about an increase in CL brightness of the Y_2O_3:Eu film [Kum99].

Shown in Figure 4-14 are the CL intensities at various electron voltages as a function of RMS roughness of the Y_2O_3:Eu thin film phosphors on anodized silicon surfaces. This figure also shows that the CL intensity increases as roughness is increased. However, the slope of the line in the figure decreases with increasing roughness of the Y_2O_3:Eu films. This is considered to have a saturation point in the graph even if the roughness increases. This kind of effect will be discussed in detail in the next chapter.

Figure 4-15 shows CL intensities of Y_2O_3:Eu thin films at 5 kV with and without a SiO_2 buffer layer between the Y_2O_3:Eu thin film phosphor and anodized silicon substrate, and demonstrates an increase in CL intensity as a SiO_2 layer is inserted. Thickness of the Y_2O_3:Eu thin films on both substrates and the SiO_2 buffer layer inserted is also 1.0 and 0.3 μm, respectively. The CL spectra appear to be consistent with the sharp PL peaks shown in Figure 4-12. The set of three closely spaced peaks at wavelengths of 587, 593, and 596 nm is related with magnetic dipole transitions ($^5D_0 - {}^7F_1$) that are insensitive to the site symmetry, whereas the peaks at 579, 610 – 630, and 680 – 710 nm are associated with electric dipole transitions ($^5D_0 - {}^7F_0$, $^5D_0 - {}^7F_2$, and $^5D_0 - {}^7F_4$, respectively) preferred by lack of inversion symmetry [For69, Rie70, Tan98]. In this figure, the Y_2O_3:Eu thin film on an anodized silicon substrate with a SiO_2 buffer showed around 30 % higher CL intensity than that of the film on the anodized silicon substrate without the buffer layer even though the roughness of anodized silicon with the buffer layer (RMS ~170 nm) was smaller than that of anodized silicon surface without it.

The CL intensities of the Y_2O_3:Eu thin film phosphors deposited on anodized silicon surfaces with a SiO_2 buffer layer for various roughness values are illustrated in Figure 4-16. It also can be seen from this figure that as the RMS roughness of the Y_2O_3:Eu films on anodized silicon surfaces with a buffer layer is increased, the CL brightness increases at all of the voltages measured as seen in Figure 4-13.

The enhanced brightness of Y_2O_3:Eu thin film phosphors on SiO_2 buffer layered silicon substrates is thought to be associated with more favorable optical properties of SiO_2 layer than those of silicon. The absorption of red light by SiO_2 buffer layer ($\alpha =$ 0.07 mm^{-1}) is much smaller than that by silicon ($\alpha >$ 200 mm^{-1}). Therefore, a significant portion of the light generated in the thin film phosphor that incidents on the silicon surface might be absorbed. In addition, due to the smaller refractive index of SiO_2 (n = 1.46) than that of Y_2O_3:Eu (n = 1.93), two different critical angles exist for total internal reflection of red light from the Y_2O_3:Eu film – SiO_2 interface (~49°) and SiO_2 – air (43°) interface. Thus, a considerable portion of the light is back reflected from the film – substrate interface and is available for escaping through the top surface, and total internal reflection cannot occur at the silicon/Y_2O_3:Eu interface since the refractive index of Si (n = 3.91) is much higher than that of Y_2O_3:Eu (n = 1.93) at a wavelength of 611 nm [Sin92, Wea98].

Summary

Silicon surfaces were anodized in aqueous HF solution controlling concentration and applied potential values in the solution to give variation in the surface roughness of the anodized silicon layer. Varying the surface roughness of silicon substrates also gave variation in the roughness of the Y_2O_3:Eu thin film phosphors to enhance the relatively low brightness of the films compared to powder phosphors.

As another approach to improving the luminescence properties, Y_2O_3:Eu thin film phosphors were deposited on anodized silicon surfaces with a SiO_2 buffer layer in order to investigate the effects of other parameters influencing the luminescence properties of the thin film phosphor.

PL and CL brightness of the thin film increased with increasing in roughness of the anodized silicon surface. The improved brightness of the thin film phosphor by means of forming an anodized silicon surface is mostly attributed to more outcoupling of light due to reduced internal reflection in the thin film phosphor. In addition, the luminescence properties of Y_2O_3:Eu films on anodized silicon surfaces with a SiO_2 buffer layer were higher than those of the films on the surface without the buffer layer. The higher brightness of the Y_2O_3:Eu thin film phosphors on SiO_2 buffer layered silicon substrate is mainly associated with the advantageous optical properties of the SiO_2 layer in terms of a smaller refractive index and a low absorption coefficient.

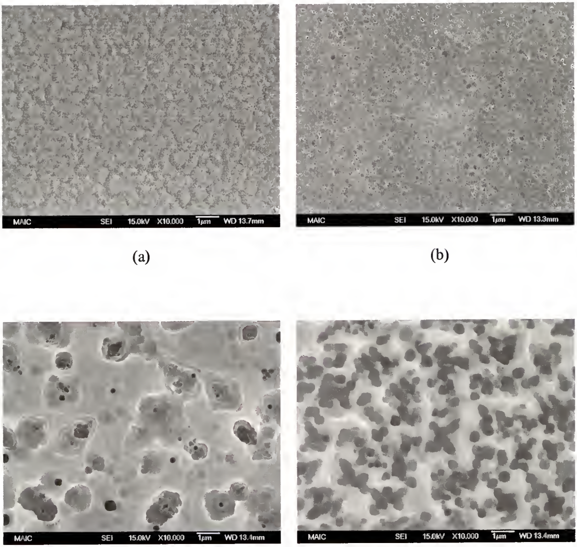
MAIC SEI 15.0kV X10,000 1μm WD 13.7mm
MAIC SEI 15.0kV X10,000 1μm WD 13.3mm
MAIC SEI 15.0kV X10,000 1μm WD 13.4mm
MAIC SEI 15.0kV X10,000 1μm WD 13.4mm

(a) (b)

(c) (d)

Figure 4-1. SEM micrographs of anodized silicon surfaces.1 % HF solution at 1 V (RMS: ~10 nm) (b) 1 % HF solution at 5 V (RMS: ~20 nm) (c) 5 % HF solution at 5 V (RMS: ~30 nm) (d) 10 % HF solution at 5 V (RMS: ~340 nm)

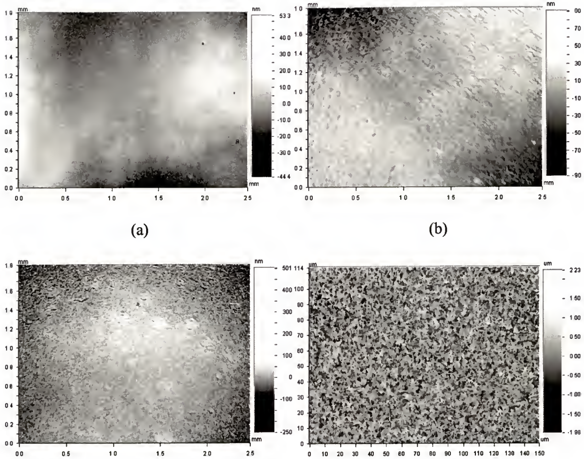

(a)

(b)

(c)

(d)

Figure 4-2. Images from an optical profilometer on anodized silicon surfaces.(a) 1 % HF solution at 1 V (RMS: ~10 nm) (b) 1 % HF solution at 5 V (RMS: ~20 nm) (c) 5 % HF solution at 5 V (RMS: ~30 nm) (d) 10 % HF solution at 5 V (RMS: ~340 nm)

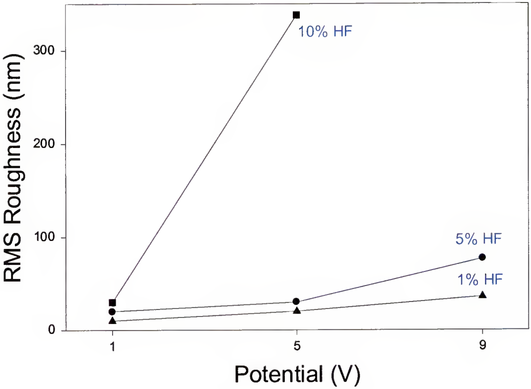

Figure 4-3. RMS roughness variation of anodized silicon surfaces with applied potential values.

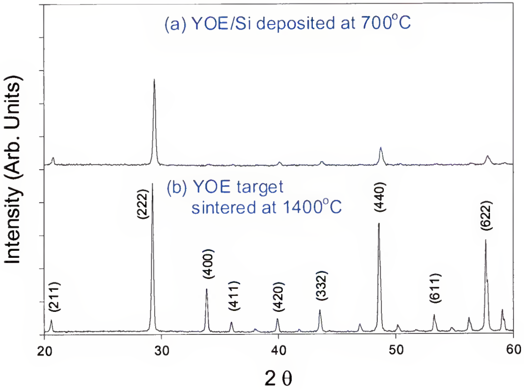

Figure 4-4. XRD patterns of (a) Y_2O_3:Eu thin films deposited on (100) anodized silicon substrate and (b) the target.

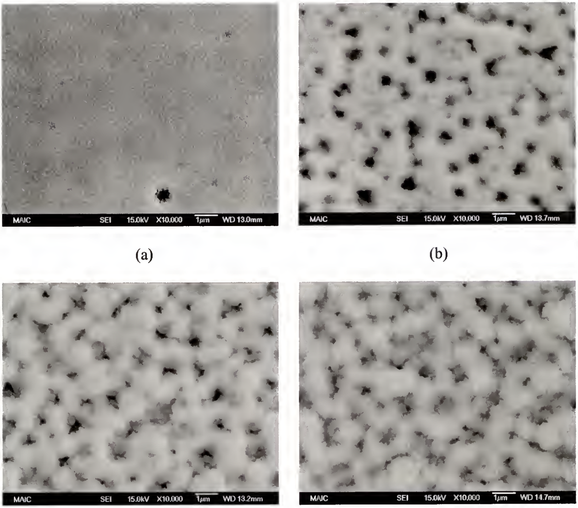
MAIC SEI 15.0kV X10,000 1μm WD 13.0mm
MAIC SEI 15.0kV X10,000 1μm WD 13.7mm
MAIC SEI 15.0kV X10,000 1μm WD 13.2mm
MAIC SEI 15.0kV X10,000 1μm WD 14.7mm

(a) (b)

(c) (d)

Figure 4-5. SEM micrographs of Y_2O_3:Eu thin films deposited on anodized silicon. RMS roughness values of ~60 nm in (a), ~120 nm in (b), ~240 nm in (c), and ~650 nm in (d).

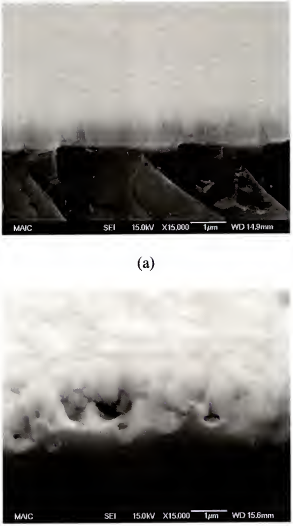

(a)

(b)

Figure 4-6. SEM cross-sectional micrographs of Y_2O_3:Eu thin films with RMS ~60 nm in (a) and RMS ~650 nm in (b) deposited on anodized silicon.

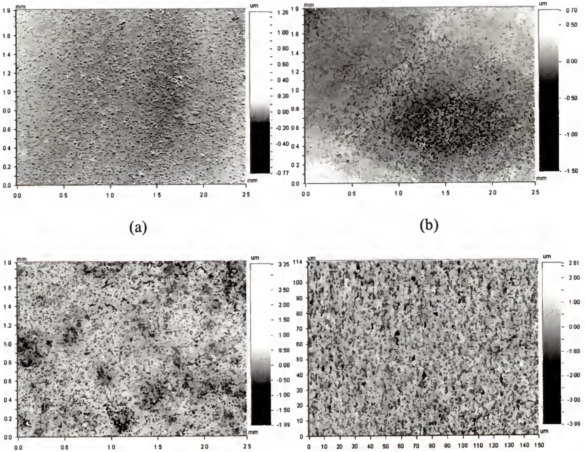

(a)

(b)

(c)

(d)

Figure 4-7. Images from an optical profilometer of Y_2O_3:Eu thin films deposited on anodized silicon surfaces. The roughness values are (a) RMS ~60 nm, (b) RMS ~120 (c), RMS ~240 nm, and (d) RMS ~650 nm.

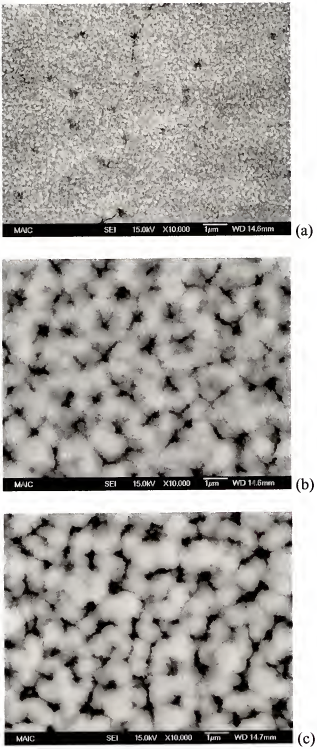
MAIC SEI 15.0kV X10,000 1μm WD 14.6mm
(a)
MAIC SEI 15.0kV X10,000 1μm WD 14.6mm
(b)
MAIC SEI 15.0kV X10,000 1μm WD 14.7mm
(c)

Figure 4-8. SEM micrographs of Y_2O_3:Eu thin films deposited on anodized silicon with SiO_2 buffer layer. The roughness values are (a) RMS ~50 nm (b) RMS ~170 nm and (c) RMS ~630 nm.

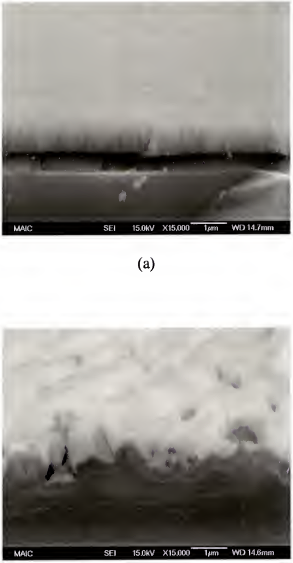

(a)

(b)

Figure 4-9. SEM cross-sectional micrographs of Y_2O_3:Eu thin films deposited on anodized silicon with a SiO_2 buffer layer. The roughness values are (a) RMS ~50 nm and (b) RMS ~630 nm.

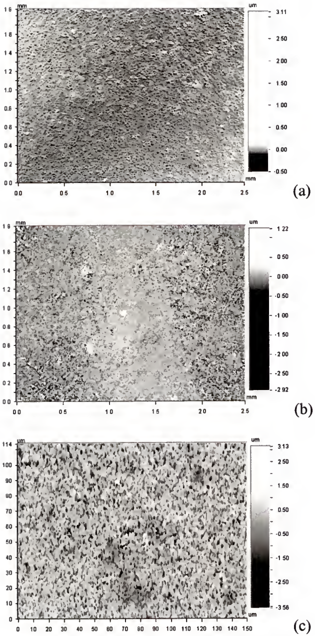

Figure 4-10. Images from an optical profilometer of Y_2O_3:Eu thin films deposited on anodized silicon surfaces with SiO_2 buffer layer. The measured roughness values are (a) RMS ~50 nm, (b) RMS ~170, and (c) RMS ~630 nm.

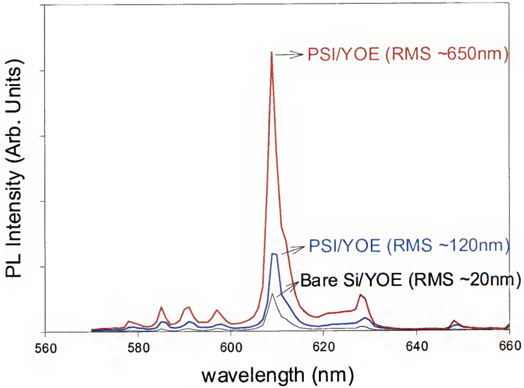

Figure 4-11. Photoluminescence intensity versus roughness of Y_2O_3:Eu thin film phosphors on the bare and anodized silicon surfaces showing increases as roughness is increased. Thickness of the Y_2O_3:Eu thin film is 1.0 μm.

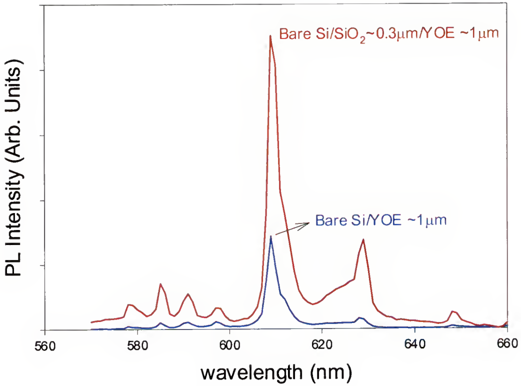

Figure 4-12. Photoluminescence intensity for Y_2O_3:Eu films with and without a SiO_2 buffer layer between the thin film phosphor and bare silicon substrate showing an increase as the SiO_2 layer is inserted. Thickness of Y_2O_3:Eu thin film and the SiO_2 buffer layer is 1.0 µm and 0.3 µm, respectively. The RMS value on both films was ~20 nm.

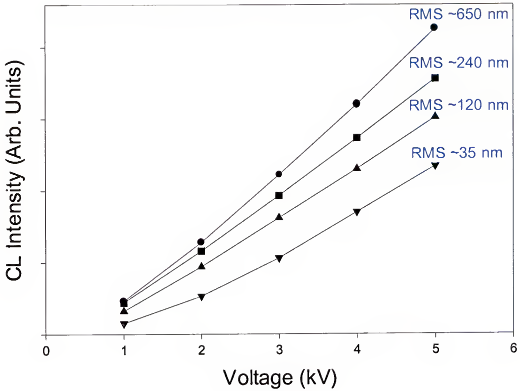

Figure 4-13. Cathodoluminescence intensity versus roughness of Y_2O_3:Eu thin film phosphors on anodized silicon surfaces at various voltages. Thickness of Y_2O_3:Eu thin films is 1.0 μm.

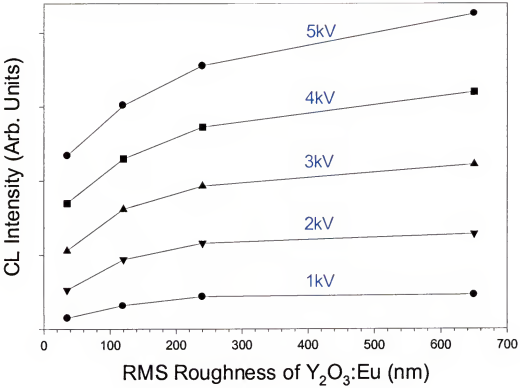

Figure 4-14. Cathodoluminescence intensity at various electron voltages versus roughness of Y_2O_3:Eu thin film phosphors on anodized silicon surfaces showing increases as roughness is increased. Thickness of Y_2O_3:Eu thin film is 1.0 μm.

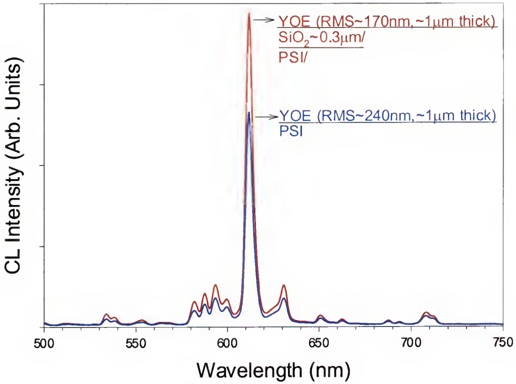

Figure 4-15. Cathodoluminescence intensities at 5 kV of Y_2O_3:Eu films with and without SiO_2 buffer layer between the thin film phosphor and anodized silicon substrate showing an increase as the SiO_2 layer is inserted. Thickness of Y_2O_3:Eu thin film and the SiO_2 buffer layer is 1.0 μm and 0.3 μm, respectively.

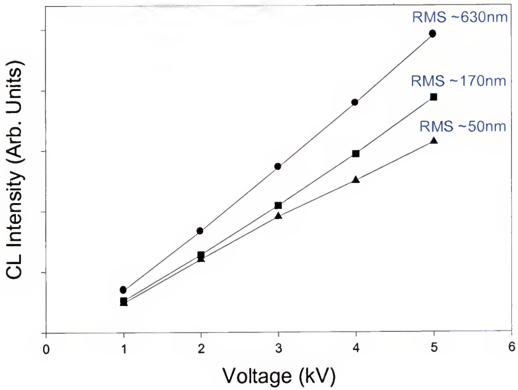

Figure 4-16. Cathodoluminescence intensity versus Y_2O_3:Eu films with SiO_2 buffer layer between the thin film phosphor and anodized silicon substrate at various voltages. Thickness of Y_2O_3:Eu thin film and the SiO_2 buffer layer is 1.0 μm and 0.3 μm, respectively.

CHAPTER 5
MODELING

Many reports have investigated to increase the brightness of thin film phosphors that is comparatively lower than that of powder phosphors by modifying the roughness of the thin film phosphors' surface. These include change in growth conditions such as substrate temperatures, growth pressure, and post-deposition annealing treatment of the phosphor films [Jon97a, b], altering thin film phosphor's surface [Lee98, Cho99], and inserting a buffer layer between the thin film phosphor and substrate [Cho98a, b]. They showed that as the surface roughness became more intense the light trapping in the phosphor layer was significantly reduced and the amount of light coming out of the layer was increased. Even though these experimental results were qualitatively comprehended well, more sufficient analysis of the scattering effects of the propagating light on the brightness of thin film phosphors is demanded.

Parameters that affect the brightness of TFPs include of film thickness, optical interfaces, microstructure, surface roughness, substrate materials, electron beam – solid interaction, and surface recombination rate. These parameters are interrelated with each other complexly and cannot be varied independently. Thus, it is hard to quantitatively elucidate the experimental results. Moreover, classical theories based on rectilinear propagation of the light cannot be applied without gross simplifications, as the wavelength of the surface roughness is smaller than the wavelength of the emitted light.

There have been some simplified models to predict the brightness of the thin film phosphors based on the effect of bulk and surface structure [Sch93, Lee98, Cho99, Jon99, Cho03]. However, they might overlook the multiple scattering at the interfaces and electron beam – solid interactions, and their solutions included only a few parameters mentioned above and cannot explain the effect of a buffer layer, that is optically favorable, on the enhanced brightness in the luminescence described in the previous chapter. Therefore, a numerical model that includes most of the affecting parameters, in particular, containing diffraction – based multiple light scatterings with different thickness of thin film phosphors and a buffer layer on various substrates and electron beam – solid interactions needs to be developed. This new model is expanded to consider a top thin film phosphor layer and substrate as well as a buffer layer between them on the basis on the previous model [Cho00, Cho03].

In this study, this numerical modeling was developed to comprehend the effects of the fundamental parameters on the luminance properties of TFPs including an optical buffer layer and develop a general solution to predict thin film-related light emission properties. This understanding and development of a numerical model will eventually lead to design for fabricating TFPs for FEDs with optimum CL properties.

Assumptions for modeling

This model is set up on the basis of the previous reports. The basic assumptions for this modeling are almost the same as Cho's [Cho00, Cho03]. The assumptions can be summarized as follows to re-enlighten fundamental optical scattering at interfaces, and the relationship between surface roughness of film and luminance intensity by diffraction scattering effects.

The model of light emission from Y_2O_3:Eu TFPs is based on the diffraction scattering of light from the various interfaces (air/film: interface 1, film/buffer layer: interface 2, buffer layer/substrate: interface 3 and substrate/air: interface 4). Figure 5-1

(a) shows the spatial distribution of the energy reflected from a rough surface with the coordinates and angle notations based on diffraction scattering theory [Bec63, Top79]. The diffraction scattering theory explains two different scattering components of the reflected light when surface roughness is smaller or comparable to the wavelength of the incident light, expressed as,

$$f(\psi,\zeta;\theta,\varphi) = f_c(\psi,\zeta;\theta,\varphi) + f_{ic}(\psi,\zeta;\theta,\varphi)\,, \tag{5.1}$$

where f is two-directional reflection coefficient, f_c is coherent (specular) component which reflects at an angle equal to the incident angle, f_{ic} is incoherent (diffuse) component which scatters in a space with some fraction of light propagating in the specular direction along with the specularly reflected light, and the definitions of the four angles (ψ, ζ, θ, ϕ) are illustrated in Figure 5-1(a). The f_c depends on the incident angle (ψ), the optical roughness (σ/λ), and the solid angle (Ω_i) containing the incident energy, while the f_{ic} depends not only on y and σ/λ but also on the direction in which the energy is reflected (θ, ϕ) and the ratio of the peak distance in Figure 5-1(b) to the wavelength of the light (a/λ) [Top79].

The generated light from each activator in the TFP, encounters absorption, diffuse and specular reflection, and diffuse and specular transmittance effects, as it traverses across the TFP. The observed brightness is the total sum intensity of the light escaping out of film surface (Reflection mode: R-mode) or substrate surface (Transmission mode: T-mode) through the multiple scattering occurring at the interfaces of 1, 2, 3, and 4. Since the roughness of the interfaces 2, 3, and 4 are very low, the diffuse effects from these interfaces are not considered. Also, the scattering effects at the grain boundaries are neglected, because significant changes in the refractive index are not expected to occur at the grain boundaries of polycrystalline structure.

Surface Roughness of Film

A sine waveform roughness is assumed for the shape of the surface roughness of the TFPs as depicted in Figure 5-1(b). From the definition of RMS roughness (σ), the relationship between the roughness height (h) and σ can be derived as

$$\sigma = \left[\frac{1}{N}\sum_{i=1}^{N}(h_i - \bar{h})^2\right]^{\frac{1}{2}} = \left[\int_0^{2\pi}\frac{A^2\sin^2\theta\, d\theta}{2\pi}\right]^{\frac{1}{2}} = \frac{A}{\sqrt{2}} = \frac{h}{2\sqrt{2}}, \quad \text{or } h = 2\sqrt{2}\sigma, \tag{5.2}$$

where $\bar{h}$ is the average roughness height with N measurements, A is the amplitude of the sine waveform roughness, and θ is the angle of the propagating light with respect to normal.

Intensity Change by an Angle Change

By definition of the solid angle (Ω) with a surface area of s in a cone of emission, the Ω is defined as

$$\Omega = \frac{s}{r^2} = \frac{2\pi rh}{r^2} = \frac{2\pi r(r - r\cos\theta)}{r^2} = 2\pi(1 - \cos\theta), \tag{5.3}$$

where r is the radius of the cone of emission, as illustrated in Figure 5-2. Then, the derivative of the Ω (the solid angle change: $d\Omega$) is the change of the cone of emission, defined as

$$d\Omega = 2\pi\sin\theta\, d\theta. \tag{5.4}$$

When light is generated in the activator center, the intensity of light (I_0) in all directions has 4π solid angle. This defines the intensity of the light of a unit solid angle as $I_0/4\pi$. Therefore, the intensity change (dI_0) by an angular element ($d\theta$) is

$$dI_0 = \frac{I_0}{4\pi} d\Omega = \frac{I_0}{4\pi} \cdot 2\pi \sin\theta\, d\theta = \frac{I_0}{2} \cdot \sin\theta\, d\theta \,. \tag{5.5}$$

Scattering of Light at Interface

When propagating light scatters at the film interface having a RMS roughness of σ, the light is divided into four different components, such as T_s, T_d, R_s, and R_d, as illustrated in Figure 5-3. From the relationship defined by Beckmann et al. [Bec63] and Toporets [Top79], the intensity of the specular reflection (I_{Rs}) can be defined as

$$I_{R_s} = I_{R_o} \exp\left[-\left(\frac{2\sqrt{2}\pi\sigma}{\lambda} \cos\theta \right)^2 \right], \tag{5.6}$$

where I_{R0} is the intensity of the internally reflecting light when $\sigma = 0$, λ is the wavelength of the generated light in the film, and θ is the angle of propagating light with respect to normal.

Figure 5-4 illustrates the assumptions for the diffuse component of the propagating light after being generated from an activator. When the light generated from an activator scatters at the interface 1, the light reflected back to the film with an angle less than θ_c ($R_d < \theta_c$) will transmit into the substrate, and the light reflected back to the film with an angle greater than θ_c ($R_d > \theta_c$) will internally reflect with another angle β, in addition to R_s. For this case, the intensity of the total internal reflection when $\sigma \neq 0$ ($I_{R\sigma \neq 0}$) is reduced by the presence of the intensity of the diffuse transmittance (I_{Td}) which is the light escaping from the film to air due to surface roughness. Then, $I_{R\sigma \neq 0}$ is defined as the sum intensity of the specularly reflected light (I_{Rs}) and the diffusely reflecting light (I_{Rd}):

$$I_{R_{\sigma \neq 0}} = I_{R_0} - I_{T_d} = I_{R_s} + I_{R_d} \,. \tag{5.7}$$

I_{Td} is a part of the I_{Rd} since the internal reflection is reduced by the existing surface roughness, thus it is defined as

$$I_{T_d} = \eta I_{R_d}, \tag{5.8}$$

where η is a constant between 0 and 1. Therefore, I_{Td} is an additional contributor to the total sum intensity of the light from the film side, in addition to the intensity of specularly transmitted light (I_{Ts}), which directly escapes from the film when θ is smaller than the critical angle, θ_c.

Equation (5.7) can be expressed for I_{Rd} by subtracting the I_{Rs} and I_{Td} from I_{R0},

$$I_{R_d} = I_{R_0} - I_{R_s} - I_{T_d}. \tag{5.9}$$

According to Beckmann et al. [Bec63] and Toporets [Top79], the I_{Rd} is also defined as

$$I_{R_d} = I_{R_0}\left[1 - \exp\left[-\left(\frac{2\sqrt{2}\pi\sigma}{\lambda}\cos\theta\right)^2\right]\right]. \tag{5.10}$$

I_{Rd} is assumed to be uniformly distributed in all directions and is expressed again using Equations (5.8) - (5.10) as

$$I_{R_d} + I_{T_d} = I_{R_0} - I_{R_s} = I_{R_0} - I_{R_0}\exp\left[-\left(\frac{2\sqrt{2}\pi\sigma}{\lambda}\cos\theta\right)^2\right], \tag{5.11}$$

$$I_{R_d} + \eta I_{R_d} = (1+\eta)I_{R_d} = I_{R_0}\left[1 - \exp\left[-\left(\frac{2\sqrt{2}\pi\sigma}{\lambda}\cos\theta\right)^2\right]\right], \tag{5.12}$$

$$\therefore\ I_{R_d} = \frac{I_{R_0}}{1+\eta}\left[1 - \exp\left[-\left(\frac{2\sqrt{2}\pi\sigma}{\lambda}\cos\theta\right)^2\right]\right]. \tag{5.13}$$

The I_{Rd} in a unit solid angle in hemisphere is defined as

$$\frac{I_{R_d}}{2\pi} = \frac{I_{R_0}}{(1+\eta)2\pi}\left[1 - \exp\left[-\left(\frac{2\sqrt{2}\pi\sigma}{\lambda}\cos\theta\right)^2\right]\right]. \tag{5.14}$$

According to Equations (5.3) and (5.4), $d\Omega$ with an angular unit $d\beta$ is

$$d\Omega = 2\pi \sin\beta \, d\beta \,. \tag{5.15}$$

Therefore, the intensities of the diffusely reflected (I_{Rd_β}) and transmitted (I_{Td_β}) light related to $d\Omega$ in Equation (5.15) are

$$I_{R_{d\_\beta}} = \frac{I_{R_d}}{2\pi} d\Omega = \frac{I_{R_0}}{(\eta + 1)}\left[1 - \exp\left[-\left(\frac{2\sqrt{2}\pi\sigma}{\lambda}\cos\theta\right)^2\right]\right]\sin\beta \, d\beta \,, \tag{5.16}$$

$$I_{T_{d\_\beta}} = \frac{\eta \, I_{R_0}}{(1 + \eta)}\left[1 - \exp\left[-\left(\frac{2\sqrt{2}\pi\sigma}{\lambda}\cos\theta\right)^2\right]\right]\sin\beta \, d\beta \,. \tag{5.17}$$

Charge Carrier Diffusion and Concentration

There are other important physical processes to be included in the model. Since CL is excited by the electron beam, which interacts differently with the solid depending on material's characteristics, accelerating voltage, and current density, it is important to predict how many charge carriers are created and involved in the luminescence process in a TFP. Since under the steady state condition the number of photons emitted is equal to the number of carriers released by the incident electrons that recombine (N). Then, a simple diffusion equation can be applied to determine the carrier concentrations in a phosphor defined as [Yoo97]

$$D\frac{d^2}{dx^2}N - \frac{N}{\tau} + G = 0 \tag{5.18}$$

where x is the depth from surface, τ is the lifetime of the radiative recombination, and G is the generation rate of the e-h pairs by e-beam. The generation rate, G, which is defined as [Yoo97],

$$G = \frac{i_0 V_0}{\Delta E R} \,, \tag{5.19}$$

where i_0 is current density, V_0 is accelerating voltage, E is average work done to create an e-h pair, and R is the interaction range of e-beam in the host matrix as defined in Equation (2.7) are also applicable to solve the diffusion equation for N. For simplification, divide each term in Equation (5.18) by D and let

$$\sqrt{\frac{1}{D\tau}} = m. \tag{5.20}$$

Then the equation can be rewritten as

$$\frac{d^2}{dx^2}N - m^2N + \frac{G}{D} = 0, \tag{5.21}$$

where m is a constant. By combining Equations (2.7) and (5.19), G can be expressed as

$$G = \frac{i_0 V_0 Z^{0.89}\rho}{27.6\Delta EME_0^{1.67}}. \tag{5.22}$$

For simplification again, let

$$C = \frac{-i_0 V_0 Z^{0.89}\rho}{\Delta E27.6ME_0^{1.67}D} = -\frac{G}{D}. \tag{5.23}$$

Then the Equation (5.21)can be rewritten as

$$\frac{d^2}{dx^2}N - m^2N = C. \tag{5.24}$$

Charge carriers can reach the activator centers outside the interaction range by diffusion. Thus two different regimes of interaction between carriers and TFP ($0<x\leq R$ and $R<x\leq 1$) should be considered in the model, as illustrated in Figure 5-9:

$$\frac{d^2}{dx^2}N_1 - m^2N_1 = C \qquad \text{for } 0 < x \leq R, \tag{5.25}$$

$$\frac{d^2}{dx^2}N_2 - m^2N_2 = 0 \qquad \text{for } R < x \leq t_1. \tag{5.26}$$

The solutions for the N_1 and N_2 are the expressions for the number of e-h pairs created in a TFP for each regime above. The solutions are given as

$$N_1 = c_1 \exp(mx) + c_2 \exp(-mx) - \frac{C}{m^2}, \tag{5.27}$$

$$N_2 = c_3 \exp(mx) + c_4 \exp(-mx), \tag{5.28}$$

where c_1, c_2, c_3, and c_4 are constants. In order to determine c_1, c_2, c_3, and c_4, the required boundary conditions are

$$(1)\quad D\left(\frac{dN_1}{dx}\right)_{x=0} = (S \cdot N_1)_{x=0} \tag{5.29}$$

$$(2)\quad \left(\frac{dN_1}{dx}\right)_{x=R} = \left(\frac{dN_2}{dx}\right)_{x=R} \tag{5.30}$$

$$(3)\quad (N_1 = N_2)_{x=t_1} \tag{5.31}$$

$$(4)\quad D\left(\frac{dN_2}{dx}\right)_{x=t_1} = -(S \cdot N_2)_{x=t_1} \tag{5.32}$$

where x is the location of the activator center to the film surface, and S is the surface recombination velocity in cm/s. Solving the four boundary conditions yields the expressions for the constants, c_1, c_2, c_3, and c_4.

Therefore, the intensity of the generated light (or brightness) can be obtained using the final solutions as:

(1) when $R>t_1$

$$\text{(a) } 0<x<t_1:\ I_0(x) = \frac{E_e}{\tau} \cdot N_1(x) \tag{5.33}$$

(2) when $R<t_1$:

$$\text{(a) } 0<x<R:\ I_0(x) = \frac{E_e}{\tau} \cdot N_1(x) \tag{5.34}$$

$$\text{(b) } R<x<t_1\text{: } I_0(x) = \frac{E_e}{\tau} \cdot N_2(x) \tag{5.35}$$

where E_e is the photon energy emitted in a TFP by an e-beam.

Modeling of Specular Component of Light

As mentioned before, the basic assumptions for this modeling is based on the previous report [Cho00, Cho03], and the equations that defined a fraction of the light transmitted from top phosphor film and substrate through multiple scattering are analogous to the equations for the top two layers, phosphor film and buffer layer underneath the film in this modeling. Therefore, the equations are summarized concisely, and then further equations are expanded.

The generated light with an intensity of I_0 from an activator, which is located at a distance of x from the film surface, propagates in all directions. A fraction of the light by changing the angular element, which is defined in Equation (5.5), can be specularly transmitted from film into air ($p_{1,2,3}$) and buffer layer ($q_{1,2,3}$) through multiple scattering between interfaces 1 and 2 during propagating upward and downward with a starting angle θ, as illustrated in Figures 5-5 (a)-(b), respectively. Some part of the light transmitted into buffer layer will be transmitted back into film through interface 2, and some other part of the light will be transmitted into buffer layer through interface 3, and further into air through interface 4, experiencing multiple scattering, as depicted in Figure 5-6(a). The light transmitted back from substrate will also experience multiple scattering in the buffer layer and the film allowing transmittance into air and substrate again, as shown in Figure 5-6(b). The intensity of the transmitted light depends on transmittance and reflectivity properties at the interfaces 1 (T_1 and R_1, respectively), 2 (T_2 and R_2, respectively), and 4 (T_4 and R_4, respectively), absorption coefficients of film (α_1), buffer layer (α_2) and substrate (α_3), and thicknesses of film (t_1), buffer layer (t_2), and substrate (t_3).

Light Propagating in Upward Direction

In Figure 5-5(a), the sum intensity of the specular components transmitted from film into air through the interface 1 ($P_1 = p_1+p_2+p_3+...+p_\infty$) can be expressed as

$$P_1 = \sum_{i=1}^{\infty} p_i = \frac{\frac{I_0}{2}\sin\theta\, d\theta\, T_1(\theta)\exp\left(\frac{-\alpha_1 x}{\cos\theta}\right)}{1 - R_1(\theta)R_2(\theta)\exp\left(\frac{-2\alpha_1 t_1}{\cos\theta}\right)\exp\left[-\left(\frac{2\sqrt{2}\pi\sigma\cos\theta}{\lambda}\right)^2\right]}. \tag{5.36}$$

The same approach can be applied to the sum intensity of the specular components transmitted from film into buffer layer through the interface 2 ($Q_1 = q_1+q_2+q_3+...+q_\infty$):

$$Q_1 = \sum_{i=1}^{\infty} q_i = \frac{\frac{I_0}{2}\sin\theta\, d\theta\, R_1(\theta)T_2(\theta)\exp\left(\frac{-\alpha_1(t_1+x)}{\cos\theta}\right)\exp\left[-\left(\frac{2\sqrt{2}\pi\sigma\cos\theta}{\lambda}\right)^2\right]}{1 - R_1(\theta)R_2(\theta)\exp\left(\frac{-2\alpha_1 t_1}{\cos\theta}\right)\exp\left[-\left(\frac{2\sqrt{2}\pi\sigma\cos\theta}{\lambda}\right)^2\right]}. \tag{5.37}$$

Light Propagating in Downward Direction

In Figure 5-5(b), the sum intensity of the specular components transmitted from film into air through the interface 1 ($P_2 = p_1+p_2+p_3+...+p_\infty$) can be expressed as

$$P_2 = \sum_{i=1}^{\infty} p_i = \frac{\frac{I_0}{2}\sin\theta\, d\theta\, R_2(\theta)T_1(\theta)\exp\left(\frac{-\alpha_1(2t_1-x)}{\cos\theta}\right)}{1 - R_1(\theta)R_2(\theta)\exp\left(\frac{-2\alpha_1 t_1}{\cos\theta}\right)\exp\left[-\left(\frac{2\sqrt{2}\pi\sigma\cos\theta}{\lambda}\right)^2\right]}. \tag{5.38}$$

The same can be applied to the sum intensity of the specular components transmitted from film into substrate through the interface 2 ($Q_2 = q_1+q_2+q_3+...+q_\infty$):

$$Q_2 = \sum_{i=1}^{\infty} q_i = \frac{\frac{I_0}{2}\sin\theta\, d\theta\, T_2(\theta)\exp\left(\frac{-\alpha_1(t_1 - x)}{\cos\theta}\right)}{1 - R_1(\theta)R_2(\theta)\exp\left(\frac{-2\alpha_1 t_1}{\cos\theta}\right)\exp\left[-\left(\frac{2\sqrt{2}\pi\sigma\cos\theta}{\lambda}\right)^2\right]}. \tag{5.39}$$

Light (I_1) Transmitted from Film into Buffer layer

In Figure 5-6(a), the sum intensity of the specular components transmitted back from buffer layer into film through the interface 2 ($P_3 = p_1+p_2+p_3+\ldots+p_\infty$) can be expressed as

$$P_3 = \sum_{i=1}^{\infty} p_i = \frac{I_1 R_3(\theta) T_2(\theta)\exp\left(\frac{-2\alpha_2 t_2}{\cos\gamma}\right)}{1 - R_2(\theta)R_3(\theta)\exp\left(\frac{-2\alpha_2 t_2}{\cos\gamma}\right)}, \tag{5.40}$$

where I_1 is the intensity of the light just after entering into the buffer layer through the interface 2, and γ is the refracted angle in the buffer layer corresponding to the incident angle θ in the film. The same method can be applied to the sum intensity of the specular components transmitted from buffer layer into substrate through the interface 3 ($Q_3 = q_1+q_2+q_3+\ldots+q_\infty$):

$$Q_3 = \sum_{i=1}^{\infty} q_i = \frac{I_1 T_3(\theta)\exp\left(\frac{-\alpha_2 t_2}{\cos\gamma}\right)}{1 - R_2(\theta)R_3(\theta)\exp\left(\frac{-2\alpha_2 t_2}{\cos\gamma}\right)}. \tag{5.41}$$

Light (I_2) Transmitted Back from Buffer layer into Film

Figure 5-6(b) shows the case of light transmitting back from buffer layer into film (I_2). The light with an intensity of I_2 will also experience multiple scattering in the film. Then, the sum intensity of the specular components transmitted from film into air through the interface 1 ($P_4 = p_1+p_2+p_3+\ldots+p_\infty$) can be expressed as

$$P_4 = \sum_{i=1}^{\infty} p_i = \frac{I_2 T_1(\theta)\exp\left(\frac{-\alpha_1 t_1}{\cos\theta}\right)}{1 - R_1(\theta)R_2(\theta)\exp\left(\frac{-2\alpha_1 t_1}{\cos\theta}\right)\exp\left[-\left(\frac{2\sqrt{2}\pi\sigma\cos\theta}{\lambda}\right)^2\right]}. \tag{5.42}$$

The same can be applied to the sum intensity of the specular components transmitted into buffer layer ($Q_4 = q_1+q_2+q_3+\ldots+q_\infty$):

$$Q_4 = \sum_{i=1}^{\infty} q_i = \frac{I_2 R_1(\theta)T_2(\theta)\exp\left(\frac{-2\alpha_1 t_1}{\cos\theta}\right)\exp\left[-\left(\frac{2\sqrt{2}\pi\sigma\cos\theta}{\lambda}\right)^2\right]}{1 - R_1(\theta)R_2(\theta)\exp\left(\frac{-2\alpha_1 t_1}{\cos\theta}\right)\exp\left[-\left(\frac{2\sqrt{2}\pi\sigma\cos\theta}{\lambda}\right)^2\right]}. \tag{5.43}$$

Light (I_3) Transmitted from Buffer layer into Substrate

In Figure 5-7(a), the sum intensity of the specular components transmitted back from substrate into buffer layer through the interface 3 ($P_5 = p_1+p_2+p_3+\ldots+p_\infty$) can be expressed as

$$P_5 = \sum_{i=1}^{\infty} p_i = \frac{I_3 R_4(\theta)T_3(\theta)\exp\left(\frac{-2\alpha_3 t_3}{\cos\delta}\right)}{1 - R_3(\theta)R_4(\theta)\exp\left(\frac{-2\alpha_3 t_3}{\cos\delta}\right)}, \tag{5.44}$$

where I_3 is the intensity of the light just after entering into the substrate through the interface 3, and δ is the refracted angle in the substrate corresponding to the incident angle γ in the buffer layer. The same method can be applied to the sum intensity of the specular components transmitted from substrate into air through the interface 4 ($Q_5 = q_1+q_2+q_3+\ldots+q_\infty$):

$$Q_5 = \sum_{i=1}^{\infty} q_i = \frac{I_3 T_4(\theta)\exp\left(\frac{-\alpha_3 t_3}{\cos\delta}\right)}{1 - R_3(\theta)R_4(\theta)\exp\left(\frac{-2\alpha_3 t_3}{\cos\delta}\right)}. \tag{5.45}$$

Light (I_4) Transmitted Back from Substrate into Buffer layer

Figure 5-7(b) shows the case of light transmitting back from substrate into buffer layer (I_4). The light with an intensity of I_4 will also experience multiple scattering in the buffer layer. Then, the sum intensity of the specular components transmitted from buffer layer into film through the interface 1 ($P_4 = p_1+p_2+p_3+\ldots+p_\infty$) can be expressed as

$$P_6 = \sum_{i=1}^{\infty} p_i = \frac{I_4 T_2(\theta)\exp\left(\dfrac{-\alpha_2 t_2}{\cos\gamma}\right)}{1 - R_2(\theta)R_3(\theta)\exp\left(\dfrac{-2\alpha_2 t_2}{\cos\gamma}\right)}. \tag{5.46}$$

The same can be applied to the sum intensity of the specular components transmitted into substrate ($Q_4 = q_1+q_2+q_3+\ldots+q_\infty$):

$$Q_6 = \sum_{i=1}^{\infty} q_i = \frac{I_4 R_2(\theta)T_3(\theta)\exp\left(\dfrac{-2\alpha_2 t_2}{\cos\gamma}\right)}{1 - R_2(\theta)R_3(\theta)\exp\left(\dfrac{-2\alpha_2 t_2}{\cos\gamma}\right)}. \tag{5.47}$$

Summation of Intensities

Now, it is necessary to consider all the above six cases together to derive the expressions for the added specular components, as illustrated in Figure 5-8 and 5-9. The sum intensity of the light transmitted from film into buffer layer for the 1st time (FB_1) in Figure 5-9 is the sum of Q_1 and Q_2 defined as

$FB_1 = Q_1 + Q_2$

$$= \frac{\dfrac{I_0}{2}\sin\theta\, d\theta\, T_2(\theta)\left[R_1(\theta)\exp\left(\dfrac{-\alpha_1(t_1+x)}{\cos\theta}\right)\exp\left[-\left(\dfrac{2\sqrt{2}\pi\sigma\cos\theta}{\lambda}\right)^2\right] + \exp\left(\dfrac{-\alpha_1(t_1-x)}{\cos\theta}\right)\right]}{1 - R_1(\theta)R_2(\theta)\exp\left(\dfrac{-2\alpha_1 t_1}{\cos\theta}\right)\exp\left[-\left(\dfrac{2\sqrt{2}\pi\sigma\cos\theta}{\lambda}\right)^2\right]}. \tag{5.48}$$

The sum intensity of light transmitted from the film into buffer layer for the 1st time (BS_1 in Figure 5-9) is comprised of the case of Q_3 when I_1 is FB_1 and the sum of all the light intensities reflecting up and down between the film and the buffer layer transmitted through the interface 2 as shown in Figure 5-8 (a) is

$$BS_1 = \Sigma BS_1'^{\times n} = FB_1Q_3 + \frac{FB_1P_3Q_4Q_3}{1-P_3Q_4} = FB_1Q_3\left(1+\frac{P_3Q_4}{1-P_3Q_4}\right), \tag{5.49}$$

where $\Sigma BS_1'^{\times n} = \Sigma(BS'_1 + BS''_1 + BS'''_1 + \cdots + BS_1'^{\times n})$.

Hereafter, the notations $P_1 \sim P_6$ and $Q_1 \sim Q_6$ in the equations below mean each summation in the equations, (5.36) ~ (5.47), without I_1, I_2, I_3, or I_4.

Next, the sum intensity of light transmitted from the substrate into buffer layer for the 1st time (SB_1 in Figure 5-9) is comprised of the case of P_5 when I_3 is BS_1 in Equation (5.44) as follows

$$SB_1 = BS_1P_5 = FB_1Q_3\left(1+\frac{P_3Q_4}{1-P_3Q_4}\right)P_5. \tag{5.50}$$

The sum intensity of light transmitted from the buffer layer into the film for the first time (BF_1 in Figure 5-9) is comprised of the case of P_6 when I_4 is SB_1 and the sum of all the light intensities reflecting up and down between the substrate and the buffer layer transmitted through the interface 3 as shown in Figure 5-8 (b) is

$$\begin{aligned} BF_1 = \Sigma BF_1'^{\times n} &= SB_1P_6 + \left(\frac{SB_1Q_6P_5}{1-Q_6P_5}\right)P_6 = SB_1P_6\left(1+\frac{Q_6P_5}{1-Q_6P_5}\right) \\ &= FB_1Q_3\left(1+\frac{P_3Q_4}{1-P_3Q_4}\right)P_5P_6\left(1+\frac{Q_6P_5}{1-Q_6P_5}\right), \end{aligned} \tag{5.51}$$

where $\Sigma BF_1'^{\times n} = \Sigma(BF'_1 + BF''_1 + BF'''_1 + \cdots + BF_1'^{\times n})$.

Let us put $\left(1+\frac{P_3Q_4}{1-P_3Q_4}\right)$ to J and $\left(1+\frac{SB_1Q_6P_5}{1-Q_6P_5}\right)$ to Y. Then, the above equations can be rewritten below

$$BS_1 = FB_1Q_3J, \tag{5.52}$$

$$SB_1 = FB_1Q_3P_5J, \tag{5.53}$$

$$\text{and } BF_1 = FB_1Q_3P_5P_6JY. \tag{5.54}$$

The equations for the sum intensity of the light transmitted from film into buffer layer for the 2nd (FB_2) and the nth time (FB_n) in Figure 5-9 are

$$FB_2 = BF_1Q_4 = SB_1P_6Q_4\left(1+\frac{Q_6P_5}{1-Q_6P_5}\right) = FB_1Q_3Q_4P_5P_6JY\,, \tag{5.55}$$

$$\text{and } FB_n = (FB_1Q_3Q_4P_5P_6JY)^{n-1}, \tag{5.56}$$

from buffer layer into substrate for the 2nd (BS_2) and the nth time (BS_n) in Figure 5-9 are

$$BS_2 = SB_1P_6Q_4\left(1+\frac{Q_6P_5}{1-Q_6P_5}\right)\left(Q_3+\frac{P_3Q_4}{1-P_3Q_4}Q_3\right)$$

$$= SB_1P_6Q_4Q_3\left(1+\frac{Q_6P_5}{1-Q_6P_5}\right)\left(1+\frac{P_3Q_4}{1-P_3Q_4}\right)$$

$$= FB_1Q_3^2Q_4P_5P_6J^2Y, \tag{5.57}$$

$$\text{and } BS_n = FB_1Q_3^nQ_4^{n-1}P_5^{n-1}P_6^{n-1}J^nY^{n-1}, \tag{5.58}$$

from substrate into buffer layer for the 2nd (SB_2) and the nth time (SB_n) in Figure 5-9 are

$$SB_2 = SB_1P_6Q_4Q_3P_5\left(1+\frac{Q_6P_5}{1-Q_6P_5}\right)\left(1+\frac{P_3Q_4}{1-P_3Q_4}\right) = FB_1Q_3^2Q_4P_5^2P_6J^2Y, \tag{5.59}$$

$$SB_n = FB_1Q_3^nQ_4^{n-1}P_5^nP_6^{n-1}J^nY^{n-1}, \tag{5.60}$$

and from buffer layer into film for the 2nd (BF_2) and the nth time (BF_n) in Figure 5-9 are

$$BF_2 = SB_1P_6Q_4Q_3P_5JYP_6 + SB_1P_6Q_4Q_3P_5P_6\,\frac{Q_6P_5}{1-Q_6P_5}$$

$$= SB_1P_6^2Q_4Q_3P_5J^2Y = FB_1Q_3^2Q_4P_5^2P_6J^2Y, \tag{5.61}$$

$$\text{and } BF_n = FB_1Q_3^nQ_4^{n-1}P_5^nP_6^{n-1}J^nY^{n-1}. \tag{5.62}$$

Therefore, the total intensities of the light specularly transmitted from substrate into buffer layer ($FB\_\theta = \Sigma\, FB_n$), of the light transmitted from buffer layer into substrate ($BS\_\theta = \Sigma\, BS_n$), of the light transmitted back from substrate into buffer layer ($SB\_\theta = \Sigma\, SB_n$), and of the light transmitted from buffer layer into film ($BF\_\theta = \Sigma\, BF_n$), started with a propagation angle of θ are

$$FB\_\theta = \frac{Q_1 + Q_2}{1 - Q_3Q_4P_5P_6JY}, \tag{5.63}$$

$$BS\_\theta = \frac{(Q_1 + Q_2)Q_3J}{1 - Q_3Q_4P_5P_6JY}, \tag{5.64}$$

$$SB\_\theta = \frac{(Q_1 + Q_2)Q_3P_5J}{1 - Q_3Q_4P_5P_6JY}, \tag{5.65}$$

$$\text{and } BF\_\theta = \frac{(Q_1 + Q_2)Q_3P_5P_6JY}{1 - Q_3Q_4P_5P_6JY}. \tag{5.66}$$

In addition, it is necessary to consider the sum intensities of the light transmit through the consecutive two layers, BF^*_θ for film/buffer layer, and BS^*_θ for buffer layer/substrate shown in Figure 5-9.

The sum of partial intensity of light transmitted back from the interface 3 into film without transmitting directly into substrate for the 1st time (BF_1^*) is the case of P_3 when I_1 is FB_1 as shown below

$$BF_1^* = FB_1P_3. \tag{5.67}$$

Then, the sum intensity of the light transmitted from film into buffer layer for the first time (FB_1^*) is the case of Q_4 when I_2 is BF^*_1 defined as

$$FB_1^* = BF_1^*Q_4 = FB_1P_3Q_4. \tag{5.68}$$

And, the sum intensities for the 2nd time are

$$BF_1^{**} = FB_1^{*}P_3 = FB_1P_3Q_4P_3 \tag{5.69}$$

$$FB_1^{**} = BF_1^{**}Q_4 \tag{5.70}$$

Therefore, the sum of $BF^{*\times n}{}_1$ that is from FB_1 becomes

$$\Sigma\, BF_1^{*\times n} = \Sigma(BF_1^{*} + BF_1^{**} + BF_1^{***} \ldots + BF_1^{*\times n}) = \frac{FB_1P_3}{1-P_3Q_4}. \tag{5.71}$$

Next, there is another sum of partial intensity of light transmitted back from the buffer layer into film without transmitting into substrate for the 1st time (BF_2^{*}) that started from FB_2 is also the case of P_3 when I_1 is FB_2 as shown in Figure 5-9 below

$$FB_2 = FB_1Q_3Q_4P_5P_6JY, \tag{5.72}$$

$$BF_2^{*} = FB_2JY = FB_1Q_3Q_4P_5P_6P_3JY. \tag{5.73}$$

Therefore, the same method can be applied to get the sum of $BF_2^{*\times n}$ that is from FB_2

$$\Sigma\, BF_2^{*\times n} = \Sigma(BF_2^{*} + BF_2^{**} + BF_2^{***} \ldots + BF_2^{*\times n}) = \frac{FB_1Q_3Q_4P_5P_6P_3JY}{1-P_3Q_4}. \tag{5.74}$$

Then, the summation of $\Sigma\, BF_1^{*\times n}$, $\Sigma\, BF_2^{*\times n} \ldots \Sigma\, BF_n^{*\times n}$ is

$$BF^{*}\_{\theta} = \Sigma\,(\Sigma\, BF_1^{*\times n} + \Sigma\, BF_2^{*\times n} + \ldots + \Sigma\, BF^{*\times n}{}_n) = \frac{\dfrac{FB_1P_3}{1-P_3Q_4}}{1-Q_3Q_4P_5P_6JY}. \tag{5.75}$$

The sum of partial intensity of light transmitted back from the interface 2 into substrate without transmitting directly into film for the 1st time (BS_1^{*}) is the case of Q_6 when I_4 is SB_1 as shown below

$$SB_1 = FB_1Q_3P_5J, \tag{5.76}$$

$$BS_1^{*} = SB_1Q_6 = FB_1Q_3P_5Q_6J. \tag{5.77}$$

Then, the sum intensity of the light transmitted from film into buffer layer for the first time (SB'_1) is the case of P_5 when I_3 is BS_1 defined as

$$SB_1^{*} = BS_1^{*}P_5 = FB_1Q_3P_5^{2}Q_6J, \tag{5.78}$$

$$BS_1^{**} = SB_1^{*}Q_6 = FB_1Q_3P_5^{2}Q_6^{2}J. \tag{5.79}$$

Therefore, the sum of $BS_1^{*\times n}$ that is from SB_1 become

$$\Sigma\, BS_1^{*\times n} = \frac{FB_1Q_3P_5Q_6J}{1-P_5Q_6}. \tag{5.80}$$

Next, there is another sum of partial intensity of light transmitted back from the buffer layer into the substrate without transmitting directly into the film for the 1st time (BS_2^{*}) that started from SB_2 is also the case of Q_6 when I_4 is SB_2 as shown in Figure 5-9 below

$$SB_2 = FB_1Q_3^{2}Q_4P_5^{2}P_6J^{2}Y, \tag{5.81}$$

$$BS_2^{*} = SB_2Q_6 = FB_1Q_3^{2}Q_4P_5^{2}P_6J^{2}YQ_6. \tag{5.82}$$

Therefore, the sum of $BS_2^{*\times n}$ that is from SB_2 become

$$\Sigma\, BS_2^{*\times n} = \frac{FB_1Q_3^{2}Q_4P_5^{2}P_6J^{2}YQ_6}{1-P_5Q_6}. \tag{5.83}$$

Then, the summation of $\Sigma\, BS_1^{*\times n}$, $\Sigma\, BS_2^{*\times n}$ … $\Sigma\, BS_n^{*\times n}$ is

$$BS^{*}_{\_\theta} = \Sigma\,(\Sigma\, BS_1^{*\times n} + \Sigma\, BS_2^{*\times n} + \ldots + \Sigma\, BS_n^{*\times n}) = \frac{\dfrac{FB_1Q_3P_5Q_6J}{1-P_5Q_6}}{1-Q_3Q_4P_5P_6JY}. \tag{5.84}$$

Finally, the total intensity of light escaping from film to air through the interface 1 (TF_{s_θ}: R-mode) is the sum of $\Sigma\, P_1$, $\Sigma\, P_2$, $BF_{\_\theta}\, P_4$, and $BF^{*}_{\_\theta}\, P_4$, and the total intensity of the light escaping from substrate to air through interface 4 (TS_{s_θ}: T-mode) started with a propagation angle of θ, is $BS_{\_\theta}\, Q_5$ and $BS^{*}_{\_\theta}\, Q_5$, expressed as

$$TF_{s\_\theta} = \Sigma P_1 + \Sigma P_2 + BF_{\_\theta} P_4 + BF^{*}_{\_\theta} P_4, \tag{5.85}$$

$$TS_{s\_\theta} = BS_{\_\theta} Q_5 + BS^{*}_{\_\theta} Q_5. \tag{5.86}$$

Integration of Specular Component

The total intensity of the generated light in the TFP with a thickness of t_1 is

$$I_{0\_total} = \int_0^{t_1} I_0 dx = I_0 t_1 , \tag{5.87}$$

assuming here that the whole thickness generates light. Therefore, the total intensity of specular light escaping from film to air (Film_s: R-mode) or from substrate to air (Substrate_s: T-mode) after generated in the film of thickness t_1, can be finalized as

$$Film_{\_s} = \int_0^{\frac{\pi}{2}} \int_0^{t_1} TF_{s\_\theta} dx d\theta , \tag{5.88}$$

$$Substrate_{\_s} = \int_0^{\frac{\pi}{2}} \int_0^{t_1} TS_{s\_\theta} dx d\theta . \tag{5.89}$$

Modeling of Diffuse Component of Light

The two achievable cases for the diffuse instances are shown in Figures 5-8(a)-(b). A component of the diffusely reflected light with an angle β initially started with an angle θ from an activator, can also propagate like a specular component of the light and this light component can also specularly transmit from film into air ($p_{1,2,3}$) and substrate ($q_{1,2,3}$) during propagating multiply upward and downward directions depending on T_1 and T_2, and R_1 and R_2 properties at the interfaces 1 and 2, respectively.

Light Propagating in Upward Direction (Diffuse)

In Figure 5-8(a), the p_1, p_2, and p_3 are the intensities of the light propagating like a specular component after first scattering at interface 1. For this case, the sum intensity of the light transmitted from film into air through the interface 1 initiated by the first diffuse reflection ($P_7 = p_1+p_2+p_3+...+p_\infty$) is

$$P_7 = \frac{\frac{I_0}{2}\sin\theta\, d\theta \exp\left(\frac{-\alpha_1 x}{\cos\theta}\right) R_1(\theta)\left(\frac{1}{1+\eta}\right)\left[1-\exp\left[-\left(\frac{2\sqrt{2}\pi\sigma}{\lambda}\cos\theta\right)^2\right]\right]\sin\beta\, d\beta\, R_2(\beta)T_1(\beta)\exp\left(\frac{-2\alpha_1 t_1}{\cos\beta}\right)}{1-R_1(\beta)R_2(\beta)\exp\left(\frac{-2\alpha_1 t_1}{\cos\beta}\right)} . \quad (5.90)$$

The same method can be applied for the sum intensity of the light transmitted from film into substrate ($Q_7 = q_1+q_2+q_3+...+q_\infty$) propagating like a specular component initiated by the first diffuse reflection at interface 1:

$$Q_7 = \frac{\frac{I_0}{2}\sin\theta\, d\theta \exp\left(\frac{-\alpha_1 x}{\cos\theta}\right) R_1(\theta)\left(\frac{1}{1+\eta}\right)\left[1-\exp\left[-\left(\frac{2\sqrt{2}\pi\sigma}{\lambda}\cos\theta\right)^2\right]\right]\sin\beta\, d\beta\, T_2(\beta)\exp\left(\frac{-\alpha_1 t_1}{\cos\beta}\right)}{1-R_1(\beta)R_2(\beta)\exp\left(\frac{-2\alpha_1 t_1}{\cos\beta}\right)} . \quad (5.91)$$

Therefore, the intensity of the diffuse transmittance from film into air by upward propagation (I_{Td_up}) can be derived as

$$I_{T_{d\_up}} = \frac{\frac{I_0}{2}\sin\theta\, d\theta \exp\left(\frac{-\alpha_1 x}{\cos\theta}\right) R_1(\theta)\left(\frac{\eta}{1+\eta}\right)\left[1-\exp\left[-\left(\frac{2\sqrt{2}\pi\sigma}{\lambda}\cos\theta\right)^2\right]\right]}{1-R_1(\theta)\exp\left[-\left(\frac{2\sqrt{2}\pi\sigma}{\lambda}\cos\theta\right)^2\right]R_2(\theta)\exp\left(\frac{-2\alpha_1 t_1}{\cos\theta}\right)} . \quad (5.92)$$

Light Propagating in Downward Direction (Diffuse)

In Figure 5-8(b), the p_1, p_2, and p_3 are the intensities of the light propagating like a specular component after reflected at interface 2 and then the first scattering at interface 1. For this case, the sum intensity of the light transmitted into air initiated by the first diffuse reflection ($P_8 = p_1+p_2+p_3+...+p_\infty$) is

$$P_8 = \frac{\frac{I_0}{2}\sin\theta\, d\theta \exp\left(\frac{-\alpha_1 (2t_1 - x)}{\cos\theta}\right) R_2(\theta)R_1(\theta)\left(\frac{1}{1+\eta}\right)\left[1-\exp\left[-\left(\frac{2\sqrt{2}\pi\sigma}{\lambda}\cos\theta\right)^2\right]\right]\sin\beta\, d\beta\, R_2(\beta)T_1(\beta)\exp\left(\frac{-2\alpha_1 t_1}{\cos\beta}\right)}{1-R_1(\beta)R_2(\beta)\exp\left(\frac{-2\alpha_1 t_1}{\cos\beta}\right)} . \quad (5.93)$$

The same approach can be applied for the sum intensity of all the light transmitted into substrate through the interface 2 ($Q_8 = q_1+q_2+q_3+\ldots+q_\infty$) propagating like a specular component initiated by the first diffuse reflection at interface 1:

$$Q_8 = \frac{\frac{I_0}{2}\sin\theta\, d\theta \exp\left(\frac{-\alpha_1(2t_1-x)}{\cos\theta}\right) R_2(\theta) R_1(\theta)\left(\frac{1}{1+\eta}\right)\left[1-\exp\left[-\left(\frac{2\sqrt{2}\pi\sigma}{\lambda}\cos\theta\right)^2\right]\right]\sin\beta\, d\beta\, T_2(\beta)\exp\left(\frac{-\alpha_1 t_1}{\cos\beta}\right)}{1-R_1(\beta)R_2(\beta)\exp\left(\frac{-2\alpha_1 t_1}{\cos\beta}\right)} . \quad (5.94)$$

Therefore, the diffuse transmittance from film into air by downward propagation (I_{Td_down}) can be derived as

$$I_{T_{d\_down}} = \frac{\frac{I_0}{2}\sin\theta\, d\theta \exp\left(\frac{-\alpha_1(2t_1-x)}{\cos\theta}\right) R_2(\theta) R_1(\theta)\left(\frac{\eta}{1+\eta}\right)\left[1-\exp\left[-\left(\frac{2\sqrt{2}\pi\sigma}{\lambda}\cos\theta\right)^2\right]\right]}{1-R_1(\theta)\exp\left[-\left(\frac{2\sqrt{2}\pi\sigma}{\lambda}\cos\theta\right)^2\right] R_2(\theta)\exp\left(\frac{-2\alpha_1 t_1}{\cos\theta}\right)} . \quad (5.95)$$

Summation of Intensities (Diffuse)

The sum intensity of the light transmitted from film into buffer layer for the 1st time (FB_1) is the sum of Q_7 and Q_8 defined as

$FB_{1d} = Q_7 + Q_8$

$$= \frac{\frac{I_0}{2}\sin\theta\, d\theta\, R_1(\theta)\left(\frac{1}{1+\eta}\right)\left[1-\exp\left[-\left(\frac{2\sqrt{2}\pi\sigma}{\lambda}\cos\theta\right)^2\right]\right]\sin\beta\, d\beta\, T_2(\beta)\exp\left(\frac{-\alpha_1 t_1}{\cos\beta}\right)\left[\exp\left(\frac{-\alpha_1 x}{\cos\theta}\right)+\exp\left(\frac{-\alpha_1(2t_1-x)}{\cos\theta}\right)R_2(\theta)\right]}{1-R_1(\beta)R_2(\beta)\exp\left(\frac{-2\alpha_1 t_1}{\cos\beta}\right)} .$$

(5.96)

This equation leads to the sum intensity of the diffuse light transmitted from film into substrate (BS_{d_β} and BS'_{d_β}) and transmitted back from substrate into film (BF_{d_β} and BF'_{d_β}) with an angle β:

$$BS_{d\_\beta} = \frac{(Q_1 + Q_2)Q_3J}{1 - Q_3Q_4P_5P_6JY}, \tag{5.97}$$

$$BS'_{d\_\beta} = \frac{\dfrac{FB_1Q_3P_5Q_6J}{1 - P_5Q_6}}{1 - Q_3Q_4P_5P_6JY}, \tag{5.98}$$

$$BF_{d\_\beta} = \frac{(Q_1 + Q_2)Q_3P_5P_6JY}{1 - Q_3Q_4P_5P_6JY}, \tag{5.99}$$

$$BF'_{d\_\beta} = \frac{\dfrac{FB_1P_3}{1 - P_3Q_4}}{1 - Q_3Q_4P_5P_6JY}. \tag{5.100}$$

The above equations look identical with the equations that are derived in the specular part previously; however, the angles used in the specular part, θ, γ, and δ, change to β, ϕ, and ϵ, respectively in the diffuse part.

Therefore, the total sum intensities of the diffuse components of the light transmitted from film into air (TF_{d_β}: R-mode), and transmitted from substrate into air (TS_{d_β}: T-mode) with an angle β are:

$$TF_{d\_\beta} = \Sigma P_7 + \Sigma P_8 + BF_{d\_\beta} P_4 + BF'_{d\_\beta} P_4, \tag{5.101}$$

$$TS_{d\_\beta} = BS_{d\_\beta} Q_5 + BS'_{d\_\beta} Q_5. \tag{5.102}$$

Finally, the total intensity of the diffuse light out of film into air (TF_{d_β}) started with a propagation angle θ is the sum of I_{Td_up}, I_{Td_down}, and the integration of TF_{d_θ} from 0 to $\pi/2$, and the total intensity of the diffuse light out of substrate into air (TS_{d_θ}) starting with an angle θ is the integration of TS_{d_β} from 0 to $\pi/2$:

$$TF_{d\_\theta} = IT_{d\_up} + IT_{d\_down} + \int_0^{\frac{\pi}{2}} TF_{d\_\beta} d\beta, \tag{5.103}$$

$$TS_{d\_\theta} = \int_0^{\frac{\pi}{2}} TS_{d\_\beta} d\beta. \tag{5.104}$$

Integration of Diffuse Component

The total generated light in a TFP with a thickness of t_1 is defined in Equation (5.87), assuming that the whole thickness generates light. Therefore, the total intensity of diffuse light escaping from film into air ($Film_{\_d}$: R-mode) or from substrate into air ($Substrate_{\_d}$: T-mode) after being generated in the film of thickness t_1, can be finalized as

$$\mathrm{Film}_{\_d} = \int_0^{\frac{\pi}{2}} \int_0^{t_1} \mathrm{TF}_{d\_\theta}\, dx d\theta\,, \tag{5.105}$$

$$\mathrm{Substrate}_{\_d} = \int_0^{\frac{\pi}{2}} \int_0^{t_1} \mathrm{TS}_{d\_\theta}\, dx d\theta\,. \tag{5.106}$$

Summation of Specular and Diffuse

The total sum intensities of the specular and diffuse from film into air (R-mode: I_{refl}), and from substrate into air (T-mode: I_{trans}) are

$$I_{refl} = \mathrm{Film}_{\_s} + \mathrm{Film}_{\_d} = \int_0^{\frac{\pi}{2}} \int_0^{t_1} \mathrm{TF}_{s\_\theta}\, dx d\theta + \int_0^{\frac{\pi}{2}} \int_0^{t_1} \mathrm{TF}_{d\_\theta}\, dx d\theta\,, \tag{5.107}$$

$$I_{trans} = \mathrm{Substrate}_{\_s} + \mathrm{Substrate}_{\_d} = \int_0^{\frac{\pi}{2}} \int_0^{t_1} \mathrm{TS}_{s\_\theta}\, dx d\theta + \int_0^{\frac{\pi}{2}} \int_0^{t_1} \mathrm{TS}_{d\_\theta}\, dx d\theta\,. \tag{5.108}$$

It is worth noting that the integration of the model equations should be considered separately for three different regimes and added up together to get total sum intensity since the TFP system has three different optical interfaces resulting in different critical angles. Therefore, each contributing part of the above equations can be written as

$$\mathrm{Film}_{\_s} = \int_0^{\theta_{c1}} \int_0^{t_1} \mathrm{TF}_{s\_\theta}\, dx d\theta + \int_{\theta_{c1}}^{\theta_{c2}} \int_0^{t_1} \mathrm{TF}_{s\_\theta}\, dx d\theta + \int_{\theta_{c2}}^{\frac{\pi}{2}} \int_0^{t_1} \mathrm{TF}_{s\_\theta}\, dx d\theta\,, \tag{5.109}$$

$$\mathrm{Film}_{\_d} = \int_0^{\theta_{c1}} \int_0^{t_1} \mathrm{TF}_{d\_\theta}\, dx d\theta + \int_{\theta_{c1}}^{\theta_{c2}} \int_0^{t_1} \mathrm{TF}_{d\_\theta}\, dx d\theta + \int_{\theta_{c2}}^{\frac{\pi}{2}} \int_0^{t_1} \mathrm{TF}_{d\_\theta}\, dx d\theta\,, \tag{5.110}$$

$$\mathrm{Substrate}_{\_s} = \int_0^{\theta_{c1}} \int_0^{t_1} \mathrm{TS}_{s\_\theta}\, dx d\theta + \int_{\theta_{c1}}^{\theta_{c2}} \int_0^{t_1} \mathrm{TS}_{s\_\theta}\, dx d\theta + \int_{\theta_{c2}}^{\frac{\pi}{2}} \int_0^{t_1} \mathrm{TS}_{s\_\theta}\, dx d\theta\,, \tag{5.111}$$

$$\text{Substrate}_{\_d} = \int_0^{\theta_{c1}} \int_0^{t_1} TS_{d\_\theta} dx d\theta + \int_{\theta_{c1}}^{\theta_{c2}} \int_0^{t_1} TS_{d\_\theta} dx d\theta + \int_{\theta_{c2}}^{\frac{\pi}{2}} \int_0^{t_1} TS_{d\_\theta} dx d\theta . \quad (5.112)$$

Each integration part of the diffuse components above should also be considered separately in three different regimes of $0<\beta<\theta_{c1}$, $\theta_{c1}<\beta<\theta_{c2}$, and $\theta_{c2}<\beta<\pi/2$, as did in the specular components.

Predicted and Experimental Results

The numerical model program automatically calculated all of the equations in this chapter step by step and gave the output data for the predicted CL intensities. All the required parameters mentioned above were input in the model to compare the predicted values with the experimental results. The parameters input for the calculation were $S = 1 \times 10^4$ cm/s, $D = 5$ cm^2/s, $\tau = 1 \times 10^{-9}$ sec, $i_0 = 100$ nA/cm^2, $\eta = 0.3$, $V_0 = 2$ kV and 5 kV, and $E = 3E_{g\text{-}Y2O3}$.

The predicted results of the CL intensities at 5 kV from the model of the Y_2O_3:Eu thin film phosphors deposited on the silicon substrates with and without SiO_2 buffer layer as a function of RMS roughness values are shown in Figure 5-11. As a whole, the normalized CL intensities in both systems of thin film phosphors increased with increasing roughness of the films up to the RMS roughness of ~ 300nm, and they appeared to be saturated after that. This saturation might be attributed to geometric effects in optics that would become more dominant as the surface roughness increased in a given incident wavelength. These predictions in the figure indicate that the Y_2O_3:Eu film on silicon substrate with a SiO_2 buffer layer gives ~ 30 % higher CL intensity than that of the silicon substrate without the buffer layer. These results are in good agreement with the experimental data as described in the previous chapter. The smaller refractive index of the SiO_2 buffer layer gives larger amount of internally reflected light in the thin film phosphor and this internally reflected light can escape out of the film more easily by diffuse transmission as the film surface is rougher. Therefore, in practical design for a thin film phosphor's system, it would become important to make choice of refractive indices of a thin film phosphor and a buffer layer, and a surface roughness value of the film. It can be suggested that a refractive index of a buffer layer should be lower than that of a thin film phosphor and a surface roughness value of a thin film phosphor should be around 300 nm (RMS) from this model.

Figure 5-12 shows the predicted and the experimental results of the CL intensities of the Y_2O_3:Eu thin film phosphors deposited on the anodized silicon substrates without SiO_2 buffer layer as a function of RMS roughness. The experimental and the predicted CL intensities were normalized by the CL intensity of the highest roughness at 5 kV to compare the trends of the both predicted and experimental CL intensities at 2 and 5 kV. As a whole, the results in this figure predicted by the model and obtained by the experiment show not much discrepancy between them. The reason why the higher CL intensities at 5 kV can be ascribed to the larger electron – solid interaction range of the higher electron energy as explained in the previous chapter. The CL intensities of experimental results at 2 kV were observed lower than those of modeling results as the RMS roughness increased. This might be mainly attributed to the surface recombination rate value that was assumed to be constant ($S = 1 \times 10^4$ cm/s) for these results, but the surface recombination rate increases as the surface roughness increases due to the increase of surface area. In other words, the effect of the recombination rate on the CL intensities of the higher voltage (5 kV) became less dominant compared to the lower voltage (2 kV) because the electron – solid interaction volume was larger than that of the lower voltage. From this figure, it can be estimated that the influence of the interface 2 (Y_2O_3:Eu/anodized Si) roughness, that was not considered in the assumptions for this model, on the CL intensities is not significant even though there is, in fact, rough interface between the film and the substrate. This can be explained by critical angle for total internal reflection. There is no light reflecting back from the interface 2 since critical angle for total internal reflection does not exist between Y_2O_3:Eu and silicon. Thus, light transmitting from the Y_2O_3:Eu thin film into silicon substrate is absorbed by the substrate, and the effect of roughness on this interface can be neglected.

Shown in Figure 5-12 are the predicted and the experimental results of the CL intensities of the Y_2O_3:Eu thin film phosphors deposited on the anodized silicon substrates with SiO_2 buffer layer as a function of RMS roughness. The experimental and the predicted CL intensities were also normalized by the CL intensity of the highest roughness at 5 kV. There is not much difference between the results of experiment and the modeling as in Figure 5-12 for the most part. The lower CL intensities of experimental data at 2 kV could be ascribed to the recombination rate as described before. Similar trends were observed at applied voltages such as saturation at around RMS 300 nm. Therefore, it can be deduced that roughness of interfaces (2: phosphor film/buffer layer and 3: buffer layer/substrate) does not have an effect on the CL intensities from these results.

However, it cannot be concluded by the data presented here that the effects of interface roughness in buffer layered thin film phosphor systems on the CL intensities may be ignored. This numerical model considered only the top roughness of thin film phosphors and the experiments were performed on silicon substrates that are not transparent to apply to FEDs.

Therefore, in order to utilize the benefits of the numerical model developed so far, transparent substrates should be used for deposition of thin film phosphors in the first place as a future work. In addition, the model should be modified to take into account effects of interface roughness on CL intensities.

Summary

A numerical model that includes most of the affecting parameters, in particular, containing diffraction – based multiple light scatterings with different thickness of thin film phosphors with a buffer layer on various substrates and electron beam – solid interactions was developed. This new model was expanded to evaluate the CL properties of the TFP/buffer layer/substrate structure on the basis of the previous model in order to comprehend the effects of the fundamental parameters on the luminescence properties of TFPs. Furthermore, the modeling developed in this study will provide many opportunities and tools in design for thin film phosphors and will be expected to play a role in fabrication of FEDs.

In summary, it was shown that only a slight difference has been observed between the predicted and the experimental results. The CL intensities were enhanced with an increase of the surface roughness of the thin film phosphors on silicon substrates. This enhanced brightness from the films on silicon surfaces was associated with the surface roughness mostly caused by the formation of the anodized silicon surface layer. Higher CL intensities from the Y_2O_3:Eu thin films on silicon with SiO_2 buffer layer were predicted. The smaller refractive index of the SiO_2 buffer layer gives larger amount of internally reflected light in the thin film phosphor and this internally reflected light can escape out of the film more easily by diffuse transmission as the film surface is rougher.

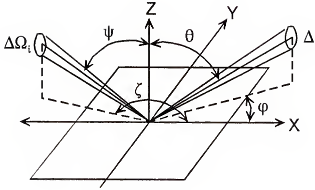

(a)

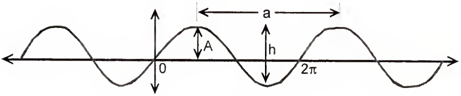

(b)

Figure 5-1. (a) Spatial distribution of the energy reflected from a rough surface with the coordinates and angle notations based on diffraction scattering theory [Top79], (b) A sine waveform roughness where A is the amplitude of the waveform, a is the distance between the two peaks, and h is the roughness height.

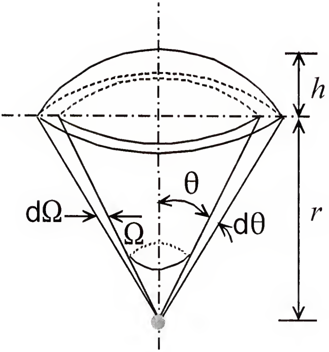

Figure 5-2. The solid angle (Ω) is defined as the ratio of surface area (s) to the square of a radius (r^2) of a cone.

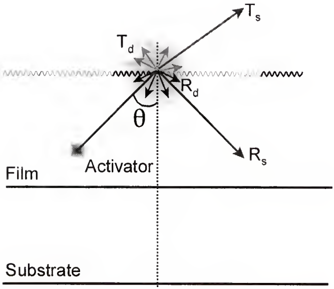

Figure 5-3. The light originated from an activator travels through the host matrix with an angle 2 and scatters at the rough film surface. This scattered light is composed of specularly reflected (R_s), diffusely reflected (R_d), specularly transmitted (T_s), and diffusely transmitted (T_d) light.

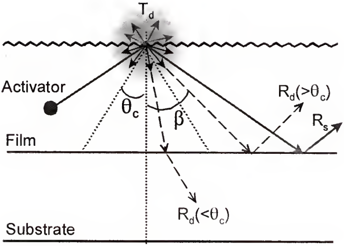

Figure 5-4. When the light generated from an activator diffusely transmits (T_d) and reflects (R_d) at the rough film surface, the light reflected back to film with an angle less than θ_c will transmit into substrate, and the light reflected back to film with an angle greater than θ_c will reflect internally with an angle β, in addition to specularly reflected light (R_s).

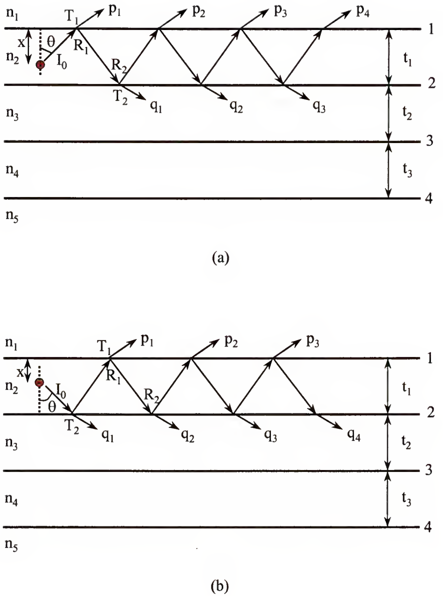

Figure 5-5. The generated light from an activator (I_0) which is located at a distance x from the film surface can be specularly transmitted from film into air ($p_{1,2,3}$) and buffer layer ($q_{1,2,3}$) during traveling (a) upward and (b) downward with an angle θ, depending on transmittance (T_1, T_2) and reflectivity (R_1, R_2) properties at the interfaces (1,2). α, n, and t represent absorption coefficient, refractive index, and thickness, respectively.

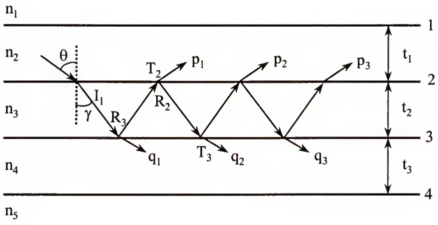

(a)

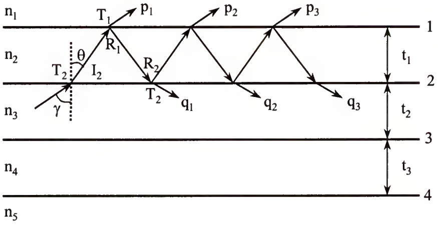

(b)

Figure 5-6. (a) The light transmitted from film into buffer layer (I_1) can be specularly transmitted from buffer layer into air ($q_{1,2,3}$) and also back-transmitted from buffer layer into film ($p_{1,2,3}$). (b) The light transmitted from buffer layer into film (I_2) can be specularly transmitted from film into air ($p_{1,2,3}$) and also back-transmitted from film into buffer layer ($q_{1,2,3}$). For both cases, light intensity depends on transmittance (T), reflectivity (R) at the interfaces (1,2,3,4), absorption coefficient ($\alpha_{1,2,3}$), thickness ($t_{1,2,3}$), and the angle θ.

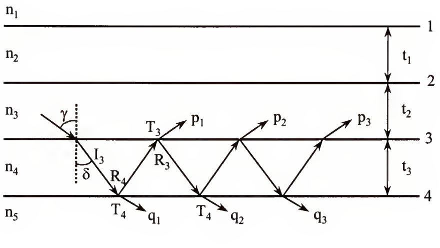

(a)

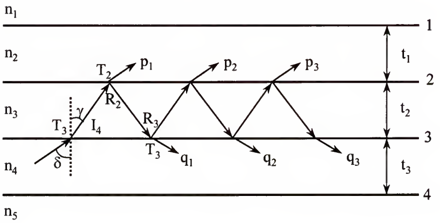

(b)

Figure 5-7. (a) The light transmitted from buffer layer into substrate (I_3) can be specularly transmitted from substrate into air ($q_{1,2,3}$) and also back-transmitted from substrate into buffer layer ($p_{1,2,3}$). (b) The light transmitted from substrate into buffer layer (I_4) can be specularly transmitted from buffer layer into film ($p_{1,2,3}$) and also back-transmitted from buffer layer into substrate ($q_{1,2,3}$). For both cases, light intensity depends on transmittance (T), reflectivity (R) at the interfaces (1,2,3,4), absorption coefficient ($\alpha_{1,2,3}$), thickness ($t_{1,2,3}$), and the angle θ.

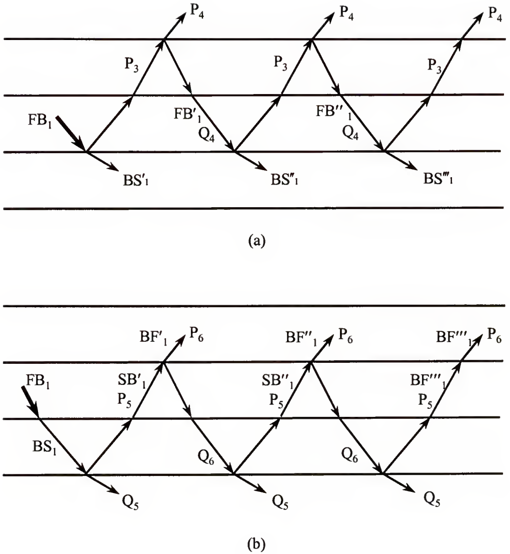

Figure 5-8. The sum of light specularly transmitted (a) from buffer layer into substrate for the first time (BS'_1), second time (BS''_1), and so on and (b) from buffer layer into film for the first time (BF'_1), second time (BF''_1), and so on, can be added together.

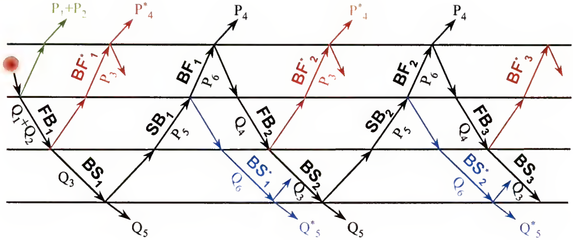

Figure 5-9. The sum of light specularly transmitted from buffer layer into substrate for the first time (BS_1), second time (BS_2), third time (BS_3), and so on, can be added together. The same applies for the sum of light specularly transmitted from buffer layer into film ($BF_{1,2,3,\ldots}$). The sum of all $P_{1,2,4}$ and P^*_4 is total specular light from film side, and the sum of all Q_5 and Q^*_5 is total specular light from substrate side.

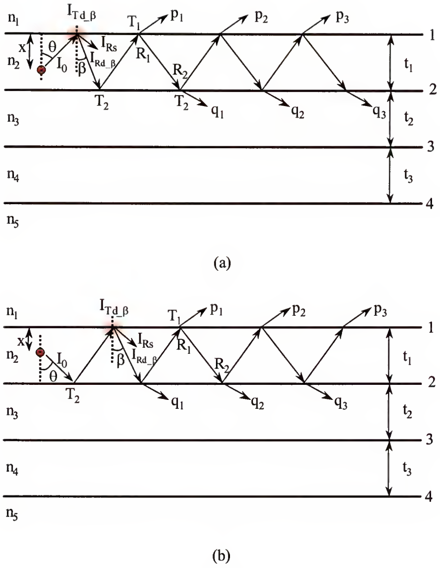

Figure 5-10. The diffusely reflected light with an angle β originally started with an angle θ, can also travels like specular component of the light and this light can also specularly transmits from film into air ($p_{1,2,3}$) and buffer layer ($q_{1,2,3}$) during traveling (a) upward and (b) downward, depending on transmittance (T_1, T_2) and reflectivity (R_1, R_2) properties at the interfaces (1,2).

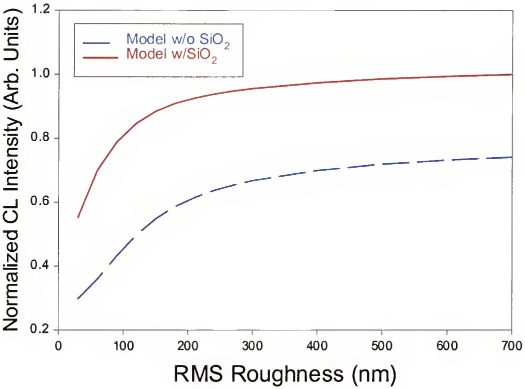

Figure 5-11. Comparison of the predicted CL intensities of Y_2O_3:Eu thin film phosphors on silicon substrates with and without SiO_2 buffer layer at 5 kV as a function of RMS.

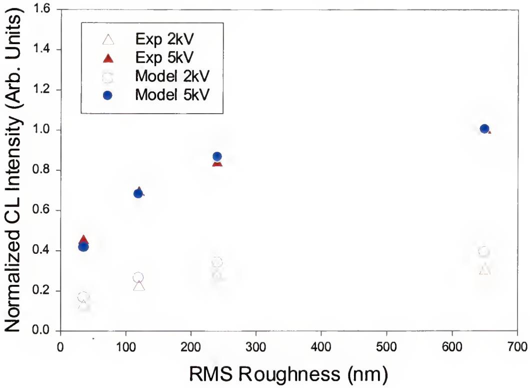

Figure 5-12. Predicted and experimental CL intensities of Y_2O_3:Eu thin film phosphors at 2 and 5 kV deposited on anodized silicon substrates as a function of RMS.

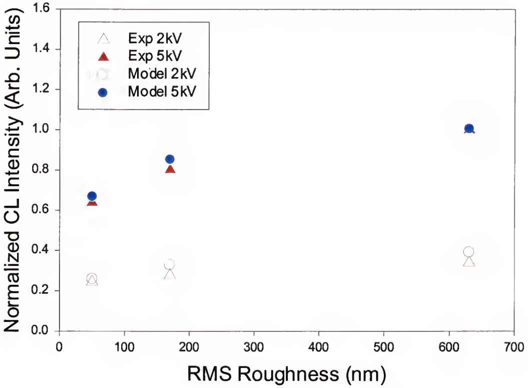

Figure 5-13. Predicted and experimental CL intensities of Y_2O_3:Eu thin film phosphors at 2 and 5 kV deposited on anodized silicon substrates with SiO_2 buffer layer as a function of RMS.

CHAPTER 6
CONCLUSIONS

The effects of surface roughness on the luminescence properties of TFPs have been investigated using PLD with Y_2O_3:Eu TFPs grown on anodized and bare silicon substrates, and also, the effect of optically favorable buffer layer was inserted between the thin film phosphor and silicon substrates. The Y_2O_3:Eu TFPs on anodized silicon substrates showed at least 2 times higher PL brightness values than those on bare silicon substrates. The realization of the Y_2O_3:Eu TFPs with higher PL brightness values by means of an inherently rough anodized silicon layer, was mainly attributed to more outcoupling of light due to reduced internal reflection.

For more detailed studies on the effects of the thin film phosphor roughness with other fundamental parameters determining the luminescence properties of the thin film phosphors, the Y_2O_3:Eu TFPs with different thicknesses and roughnesses were fabricated using PLD on the substrate materials that have various roughness values under a controlled experimental procedure. Microstructural and optical characterizations were conducted on those samples. The PL brightness of the Y_2O_3:Eu thin film phosphors deposited on the anodized silicon substrates increased with the surface roughness of the film and the thickness of SiO_2 buffer layer. The new theoretical model also explains this result.

The smaller refractive index and low absorption coefficient characteristics of the SiO_2 buffer layer on the substrates resulted in higher CL intensities in both theoretical and experimental results for the Y_2O_3:Eu TFP systems. The smaller refractive index of the buffer layer produced larger amount of internally reflected light in the film and this internally reflected light escaped from the film more easily as the film surface is rougher. The low absorption of visible light by the SiO_2 buffer layer also decreased light intensity losses during multiple internal reflections. These two combined effects resulted in better PL properties for the Y_2O_3:Eu TFPs on SiO_2 buffer layered silicon substrate.

The theoretical model provides solid understandings on the CL properties of the thin film phosphors with the effects of the various parameters, in terms of the role of surface roughness and the role of the buffer layer on reducing internal reflection, and the correlations of the surface roughness with other parameters such as substrate types, e-beam-solid interactions, surface recombination rates of carriers, carrier diffusion properties, optical scattering at the interfaces, and material's optical properties. Therefore, the new model supplies a general solution to predict the luminescence properties of the thin film phosphors for the CL – based technologies like FEDs and CRTs.

LIST OF REFERENCES

And70 R. C. Anderson, Refractory Materials, edited by A. M. Alper, Academic, New York, 1 (1970).

Bea72 D. R. Beaman and J. A. Isasi, Electron Beam Microanalysis, ASTM Special Publication 506, Philadelphia: American Society for Testing and Materials (1972).

Bla94 G. Blasse and B. C. Grabmaier, Luminescent Materials, Springer-Verlag, Berlin (1994).

Bro64 I. Brodie, J. Appl. Phys., 35, 2324 (1964).

Bru92 C. R. Brundle, C. A. Evans, and S. Wilson, Encyclopedia of Materials Characterization, Manning Publications Incorporated, Greenwich, Connecticut. (1992).

Can87 L. Canham, Properties of Porous Silicon, IEE, INSPEC, London, U.K. (1987).

Cat95 D. A. Cathey, Journal of SID, 16 (1995).

Cha90 C. C. Chang, X. D. Wu, R. Ramesh, X. X. Xi, T. S. Ravi, T. Venkatesan, D. M. Hwang, R. Muenchausen, S. Foltyn, and N. S. Nogar, Appl. Phys. Lett., 57, 1874 (1990).

Cho97 K. G. Cho, D. Kumar, D. G. Lee, S. L. Jones, P. H. Holloway, and R. K. Singh, Appl. Phys. Lett., 71 (23), 3335 (1997).

Cho98a K. G. Cho, D. Kumar, S. L. Jones, D. G. Lee, P. H. Holloway, and R. K. Singh, J. Electrochem. Soc., 145, 3456 (1998).

Cho98b K. G. Cho, D. Kumar, P. H. Holloway, and R. K. Singh, Advances in laser ablation of materials 1998, edited by R. K. Singh, D. H. Lowndes, D. B. Chrisey, J. Narayan, T. Kawai, and E. Fogarass, MRS Symp. Proc., 526, 317 (1998).

Cho99 K. G. Cho, D. Kumar, Z. Chen, P. H. Holloway, and R. K. Singh, Flat panel displays and sensors (principles, materials, and processes) 1999, edited by F.R. Libsch, B. Chalamala, R. Friend, T. Jackson, and H. Ohshima, MRS Symp. Proc., 558, Spring meeting (1999).

Cho00 K. G. Cho, Ph. D. Dissertation, Gainesville, FL, University of Florida (2000).

Cho03 K. G. Cho, J. Choi, Z. Chen, and R. K. Singh, Phys. Rev. B, submitted.

Cou96 F. Courreges, Information Display, 12, 10 (1996).

Cra93 W. M. Crantom, D. M. Spink, R. Stevens, and C. B.Thomas, Thin Solid Films, 226, 156 (1993).

Czy90 Z. Czyewski, D. O. N. MacCallum, A. Romig, and D. C. Joy, J. Appl. Phys., 68, 3066 (1990).

Duc94 S. J. Duclos, C. D. Greskovich, and O'Clair, C. R. Scintillators and phosphor materials, edited by M. J. Weber, P. Lecoq, R. C. Ruchti, C. Woody, W. M. Yen, and R. Y. Zhu, MRS Symp. Proc., 348, 503 (1994).

Eve71 T. E. Everhart and P. H. Hoff, J. Appl. Phys., 42, 5837 (1971).

Fol94 S. R. Foltyn, Pulsed Laser Deposition of Thin Films, edited by D. Crisey, G. K. Hubler, John Wiley and Sons, New York, NY, (1994).

For69 H. Forest and G. Ban, J. Electrochem. Soc., 116 (4), 474 (1969).

Gas89 F. Gaspard, A. Bsiesy, M. Ligeon, F. Muller, and R. Herino, J. Electrochem. Soc.,136, 3043 (1989).

Gol92 J. I. Goldstein, D. E. Newbury, P. Echlin, D. C. Joy, A. D. Romig, C. E. Lyman, C. Fiori, E. Lifshin, Scanning Electron Microscopy and X-Ray Microanalysis, Plenum Press, New York, NY, (1992).

Gue96 Y. M. Gueorguiev, D. I. Ivanov, and G. M. Mladenov, Vacuum, 47, 1227 (1996).

Hol96 P. H. Holloway, J. S. Sebastian, T. A. Trottier, S. L. Jones, H. Swart, and R. O. Peterson, Flat Panel Display Materials II, MRS Proceedings, Pittsburgh, PA, 424 (1996).

Hol99 P. H. Holloway, T. A. Trottier, B. Abrams, C. Kondoleon, S. L. Jones, J. S. Sebastian, W. J. Thomas, and H. Swart, J. Vac. Sci. Technol., B 17(2), 758 (1999).

Hud92 J. B. Hudson, Surface Science An Introduction, Butterworth-Heinemann, Stoneham, MA. (1992).

Hun85 R. B. Hunt, and R. G. Pappalardo, J. Luminescence, 34, 133 (1985).

Ito89 S. Itoh, T. Kimizuka, and T. Tonegawa, J. Electrochem. Soc., 136, 1819 (1989).

Jan93 A. F. Jankowski, L. R. Schrawyer, and J. P. Hayes, J. Vac. Sci. Technol. A, 11, 1548 (1993).

Jon97a S. L. Jones, D. Kumar, R. K. Singh, and P. H. Holloway, Appl. Phys. Lett., 71 (3), 404 (1997).

Jon97b S. L. Jones, D. Kumar, R. K. Singh, and P. H. Holloway, Flat Panel Display Materials III, edited by R. T. Fulks, G. N. Parsons, D. E. Slobod, and T. H. Yuzuriha. MRS Symp. Proc. 471, 299 (1997).

Jon97c S. L. Jones, Ph. D. Dissertation, Gainesville, FL, University of Florida (1997).

Jon99 S. L. Jones, D. Kumar, K. G. Cho, R. K. Singh, and P. H. Holloway, Displays 19, 151 (1999).

Joy89 D. C. Joy and S. Luo, Scanning, 11, 176 (1989).

Kim97 J. M. Kim, J. P. Hong, J. W. Kim, J. H. Choi, N. S. Park, J. H. Kang, J. E. Jang, Y. S. Ryu, H. C. Yang, B. I. Gorfinkel, and E. V. Roussina, J. Vac. Sci. Technol., B 15 (2), 528 (1997).

Kin70 J. D. Kingsley, and G. W. Ludwig, J. Electrochem. Soc., 117 353 (1970).

Kor99 Ed Korczynski, Solid State Technology (January), 51 (1999).

Kum99 D. Kumar, K. G. Cho, Z. Chen, P. H. Holloway, and R. K. Singh, Phys. Rev. B 60 (19), 13331 (1999).

Lee98 Song Jae Lee, Jpn. J. Appl. Phys., 37, 509 (1998).

Mae92 P. Maestro, D. Huguenin, A. Seigneurin, F. Deneuve, P. L. Lam, and J. F. Berar, J. Electrochem. Soc., 139 (5), 1479 (1992).

Mar88 D. J. Marshall, Cathodoluminescence of Geological Materials, Unwin Hyman, Boston, 1-16 (1988).

Mem66 R. Memming and G. Schwandt, Surf. Sci., 105, 402 (1966).

Off95 Office of Technology Assessment, U.S. Congress, Flat panel displays in perspective, OTA-ITC-631. U.S. Government Printing Office, Washington DC, September (1995).

Oni90 K. I. Onisawa, M. Fuyama, K. Tamura, K. Taguchi, T. Nakayama, and Y. A. Ono, J. Appl. Phys., 68 (2), 719 (1990).

Pin64 D. Pines, Elementary Excitation in Solids, W.A. Benjamin, New York, (1964).

Rao74 T. S. Rao-Sahib and D. B. Wittry, J. Appl. Phys., 45, 5060 (1974).

Rao96 R. P. Rao, Solid State Communications, 99 (6), 439 (1996).

Reu00 R. H. Reuss and B. R. Chalamala, Mat. Res. Soc. Symp. Proc., 558, 49 (2000).

Rie70 E. P. Riedel. J. Luminescence 1-2, 176 (1970).

Ron98 C. R. Ronda, T. Jüstel, and H. Nikol, J. Alloys and Comp., 275~277, 669 (1998).

Rou94 J. Rouquerol, D. Avnir, C. W. Fairbridge, D. H. Everett, J. H. Haynes, N. Pernicone, J. D. F. Ramsay, K. S. W. Sing, K. K. Unger, Pure Appl. Chem., 66, 1739 (1994).

Sch93 I. Schnitzer and E. Yablonovitch, Appl. Phys. Lett., 63 (16), 2174 (1993).

Sch95 P. R. Schwoebel, and I. Brodie, J. Vac. Sci. Technol., B 13 (4), 1391 (1995).

Sea92a P. Searson, J. Macaulay, and S. Prokes, J. Electrochem. Soc., 139, 3373 (1992).

Sea92b P. Searson, J. Macaulay, and F. Ross, J. Appl. Phys., 72, 253 (1992).

Sha91 R. N. Sharma, S. T. Lakshami, and A. C. Rastogi, Thin Solid Films, 199, 1 (1991).

She98 L. E. Shea, Interface, 7 (2), 24 (1998).

Sin02 R. K. Singh, Z. Chen, D. Kumar, K. Cho, and M. Ollinger, Appl. Surf. Sci., 197 – 198, 321 (2002).

Smi92 R. L. Smith and S. D. Collins, J. Appl. Phys., 71, R1 (1992).

Smi98 R. T. Smith, Information Display, 2/98, 12 (1998).

Swa96 H. C. Swart, J. S. Sebaschian, T. A. Trottier, S. L. Jones, and P. H. Holloway, J. Vac. Sci. Technol., A13, 1697 (1996).

Tan98 S. Tanimizu, Phosphor handbook, edited by S. Shionoya and W. M. Yen. CRC, Boca Raton, FL, 141 (1998).

Tro97 T. A. Trottier, Ph.D. Dissertation, Gainesville, FL: University of Florida, (1997).

Tur58 D. Turner, J. Electrochem. Soc., 105, 402 (1958).

Uhl56 A. Uhlir, Bell System Tech. J., 35, 333 (1956).

Vec99 A. Vecht, C. Gibbons, D. Davies, X. Jing, P. Marsh, T. Ireland, J. Silver, A. Newport, and D. Barber, J. Vac. Sci. Technol., B 17(2), 750 (1999).

Wea98 J. H. Weaver and H. P. R. Frederikse, CRC Handbook of Chemistry and Physics, 78th ed. Edited by D. R. Lide and H. P. R. Frederikse, CRC press, New York (1998).

Wic64 K. A. Wickersheim and R. A. Lefever, J. Electrochem. Soc., 111(1), 47 (1964).

Wil93 C. Wild, P. Koidl, W. Muller-Sebert, H. Walcher, R. Kohl, N. Herres, R. Rocher, R. Samlenski, and R. Brenn, Diamond and Related Mater., 2, 158 (1993).

Yac90 B. G. Yacobi and D. B. Holt, Cathodoluminescence Microscopy of Inorganic Solids. Plenum, New York, 1 (1990).

Yos98 T. Yoshioka and M. Ogawa, Phosphor Handbook, edited by S. Shionoya and W. M. Yen. CRC, Boca Raton, 683-726 (1998).

Zac97 M. Zachau, J. Luminescence, 72-74, 792 (1997).

BIOGRAPHICAL SKETCH

Jaeyoung Choi was born on August 21, 1967, in Taegu, Korea. He attended Young Sin High School, where he graduated in 1986. The next six years were spent at Yonsei University, Seoul, Korea, where he graduated with a Bachelor of Science and a Master of Science degree in metallurgical engineering. Upon completion of his master's degree in August of 1993, he spent five years at Daewoo Electronics company. Then, he stayed the next five years at the University of Florida under the guidance of Dr. Rajiv Singh.

I certify that I have read this study and that in my opinion it conforms to acceptable standards of scholarly presentation and is fully adequate, in scope and quality, as a dissertation for the degree of Doctor of Philosophy.

R. K. Singh, Chair
Professor of Materials Science and
Engineering

I certify that I have read this study and that in my opinion it conforms to acceptable standards of scholarly presentation and is fully adequate, in scope and quality, as a dissertation for the degree of Doctor of Philosophy.

S. J. Pearton
Professor of Materials Science and
Engineering

I certify that I have read this study and that in my opinion it conforms to acceptable standards of scholarly presentation and is fully adequate, in scope and quality, as a dissertation for the degree of Doctor of Philosophy.

C. R. Abernathy
Professor of Materials Science and
Engineering

I certify that I have read this study and that in my opinion it conforms to acceptable standards of scholarly presentation and is fully adequate, in scope and quality, as a dissertation for the degree of Doctor of Philosophy.

D. P. Norton
Professor of Materials Science and
Engineering

I certify that I have read this study and that in my opinion it conforms to acceptable standards of scholarly presentation and is fully adequate, in scope and quality, as a dissertation for the degree of Doctor of Philosophy.

Arthur F. Hebard

A. F. Hebard
Professor of Physics

This dissertation was submitted to the Graduate Faculty of the College of Engineering and to the Graduate School and was accepted as partial fulfillment of the requirements for the degree of Doctor of Philosophy.

December 2003

Pramod Khargonekar

Pramod P. Khargonekar
Dean, College of Engineering

Winfred M. Phillips
Dean, Graduate School